Spatial analyses of exploration evidence data to model skarn-type copper prospectivity in the Varzaghan district, NW Iran

Mohammad Parsa[a], Abbas Maghsoudi[a,*], Mahyar Yousefi[b]

[a] Faculty of Mining and Metallurgical Engineering, Amirkabir University of Technology, Tehran, Iran
[b] Faculty of Engineering, Malayer University, Malayer, Iran

ARTICLE INFO

ABSTRACT

Recognition of significant ore-forming processes, which control mineralization, improves the efficiency of mineral prospectivity modeling. In this study, controlling processes of skarn copper mineralization in Varzaghan district, northwestern Iran, were distinguished by a series of spatial and numerical analyses comprising point pattern, fractal, fry and distance distribution methods. The recognized processes were then translated to a set of exploration criteria of the deposits in the area. Based on the accomplished exploration criteria, two data-driven models of skarn copper prospectivity were generated using logistic regression and random forest techniques. The comparison of two generated models demonstrated that the targets derived by the latter technique were more reliable for further exploration than those created by the former one.

1. Introduction

Mineral prospectivity mapping (MPM) endeavors to ascertain reliable exploration targets where undiscovered mineralization might be found (cf. Bonham-Carter et al., 1990; Carranza, 2008). Defining competent exploration criteria of the deposit-type sought is a fundamental task in MPM. This is achieved by weeding out inefficient criteria through inspecting the previously-discovered mineral deposits of the targeted type (e.g., Cox and Singer, 1986; Roberts et al., 1988; Pirajno, 1992). Translation of ore-forming processes of a given type of mineral deposits to a set of exploration evidence layers is another critical task in MPM (Nykänen et al., 2015; Lindsay et al., 2016). This is because mineral deposits of the same type do not form under identical geological settings (Andrada de Palomera et al., 2015; Parsa et al., 2016a,b). Therefore, the application of imprecisely-defined deposit models and the ensuing exploration evidence layers propagate systematic uncertainties to MPM (Carranza et al., 2008; Yousefi and Carranza, 2015a,b; Parsa et al., 2017a). To modulate the foregoing caveat, the exploration criteria, which were elicited from the descriptive deposit models, should be tuned to the characteristics of known mineral deposits (KMDs) of the targeted type in a given study area (Kreuzer et al., 2007; Carranza, 2008, 2009a; Lisitsin, 2015; Haddad-Martim et al., 2017).

Recognition of significant geological factors controlling mineralization of the targeted type is a critical issue for defining adjusted exploration criteria (Cox and Singer, 1986; Carlson, 1991; Pirajno, 1992; Vearncombe and Vearncombe, 1999; McCuaig et al., 2010; Kreuzer et al., 2007; Lisitsin, 2015). Analyses of the spatial distribution of mineral deposits and modeling their spatial association with exploration evidence data (e.g., geological features and geochemical indicators) provide insights to the controls on ore deposition. The former case infers the quantity and the quality of plausible controls on mineralization and the latter case identifies the exploration features which have significant spatial associations with mineralization (Carranza, 2008). Point pattern (Diggle, 1983; Boots and Getis, 1988), fractal (Mandelbrot, 1983) and fry (Fry, 1979) analyses have been applied (e.g., Carranza, 2008, 2009a; Haddad-Martim et al., 2017) for the analysis of the spatial distribution of mineral deposits. Distance distribution (Berman, 1977, 1986) and t-student spatial-statistic (Bonham-Carter et al., 1990) analyses are two widely-used methods for measuring the spatial association of mineral deposits with exploration data sets (e.g., Carranza and Sadeghi, 2010; Parsa et al., 2017a).

The main aims of this study are to (a) adjust the exploration criteria of skarn Cu deposits (SCDs) in the Varzaghan district, northwestern Iran and (b) generate an efficient data-driven mineral prospectivity model of the SCDs based on the adjusted criteria. To reach these goals, the preceding spatial analyses were conducted to infer geological controls on the deposit-type sought. Besides, multivariate geochemical analyses were applied in conjunction with the spatial analysis to recognize significant multi-element geochemical signatures of the deposit-type sought (e.g., Parsa et al., 2016a). Following the resultant consequences, a set of efficient evidence layers were generated and two data-driven
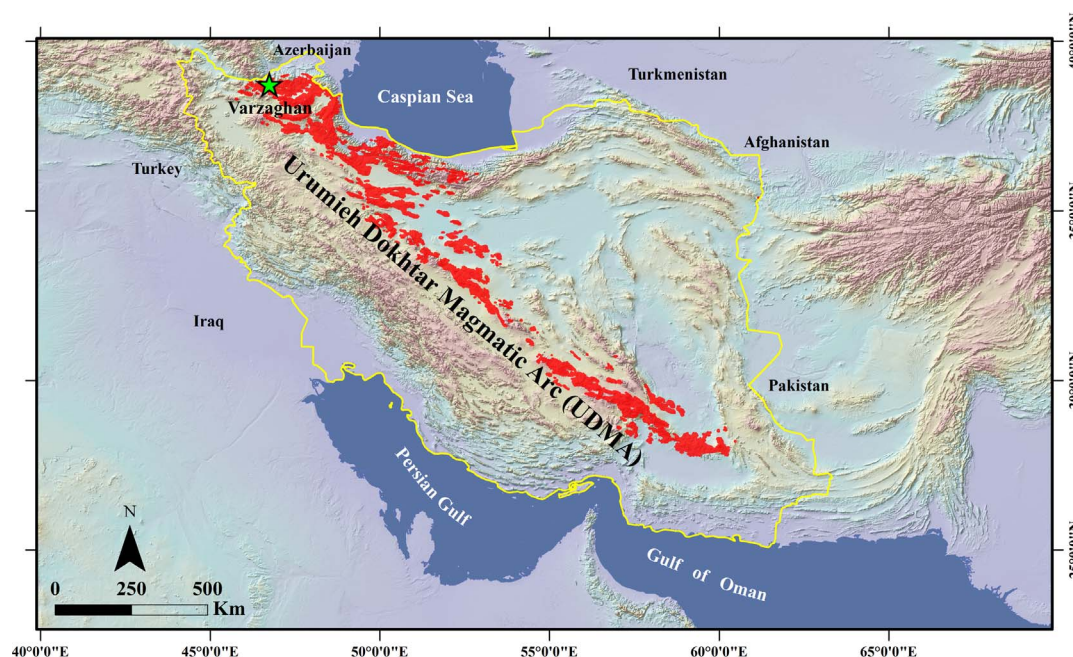

Fig. 1. Shaded relief map showing the Urumieh-Dokhtar Magmatic Arc (UDMA) and the location of study area (from Alavi, 2004). Yellow polygon depicts the territorial boundaries of Iran. (For interpretation of the references to colour in this figure legend, the reader is referred to the web version of this article.)

MPM procedures (e.g., Rodriguez-Galiano et al., 2015; Asadi et al., 2015, 2016; Carranza and Laborte, 2016; Fatehi and Asadi, 2017a,b) of logistic regression (Hosmer and Lemeshow, 2000) and random forest (Breiman, 2001) were conducted. The prospectivity models were then compared, and exploration targets were generated according to the superior prospectivity model.

2. Varzaghan district

2.1. Geological setting

The northwestern-trending Urumieh-Dokhtar Magmatic ARC (UDMA) extends over a length of 1800 km (Jamali et al., 2010; Zarasvandi et al., 2015), in which the Varzaghan district is situated (Fig. 1). Porphyry and skarn copper mineralizations dominantly occurred in the UDMA (Jamali and Mehrabi, 2015; Aghazadeh et al., 2015), making this arc favorable for prospecting further copper deposits (Hezarkhani and Williams-Jones, 1998; Richards et al., 2012).

The study area comprises about 1000 km² of the northern UDMA, which is underlain mainly by the Cretaceous limestones and Cretaceous volcano-sedimentary succession comprising intermediate lava flow, sandstone and marl (Fig. 2). In the Varzaghan district, the magmatism commenced in Eocene with the emplacement of intermediate to felsic volcanic rocks and nepheline-syenitic to monzo-syenitic plutonic rocks and continued in late Oligocene with the intrusion of coarse-grained quartz-monzonitic and granodioritic plutons (Mehrpartou et al., 1992; Mehrpartou and Nazer, 1999). The magmatic-related ore deposits (e.g., porphyry and skarn deposits) in the study area are associated with the Oligocene-Miocene intrusions whereas the Eocene intrusive rocks do not host any significant mineralization (Karimzadeh Somarin and Moayyed, 2002; Hassanpour, 2013; Jamali and Mehrabi, 2015; Aghazadeh et al., 2015). Ascending ore-bearing fluids with magmatic origin in the study area were structurally controlled, and thus fault systems were vital for the development of magmatic-related mineral systems (Aghazadeh et al., 2015). The emplacement of water-saturated Oligocene-Miocene plutons in the study area and its adjacent terrains followed a general NW-SE trend (Alavi, 1994; Mollai et al., 2009; Jamali et al., 2010), running parallel to the orientation of the UDMA. The Quaternary volcanic rocks that unconformably overlie the older

geological units of the Varzaghan district are the consequence of the latest magmatic activities in the area (Mehrpartou et al., 1992).

2.2. Geodynamic setting

The geodynamic settings of the Cenozoic magmatism and the ensuing skarn mineralization in the study area are still subjects of debates. Different models have been proposed for the tectonomagmatic evolution of the study area, some of which envisage a terminated subduction-related magmatism (e.g., Alavi, 1994, 2007; Glennie, 2000). However, the results of recent studies suggest ongoing post-collisional tectonic regimes for the magmatism of the study area (e.g., Jamali et al., 2010; Maghsoudi et al., 2014; Aghazadeh et al., 2015). In this regard, according to Aghazadeh et al. (2015), the magmatic activities in the study area were commenced by the subduction of Neo-Tethys oceanic lithosphere beneath the Central Iranian plate in late Mesozoic. This stage was yielded in the extensive emplacement of the Eocene volcanic and plutonic rocks and was succeeded by the closure of Neo-Tethys and subsequent collision between the Arabian plate and Central Iranian plate in the late Eocene. Following the termination of Eocene magmatism, the Central Iranian crust thickened which led to the detachment of the lithospheric mantle from the upper lithosphere and subsequent sinking into the asthenosphere. The remaining lithosphere then triggered the development of the fertile Oligocene-Miocene intrusions and the subsequent mineralization of the study area.

2.3. Skarn copper mineralization

Skarn deposits are among the crucial resources of Cu, Fe, Zn and W commodities (Burt, 1977). These types of mineralization have been emplaced in orogenic belts with high-temperature hydrothermal activities (Meinert, 1992; Meinert et al., 2005). In these deposits, mass and heat have been transported from cooling magmas to the calcareous sedimentary wall rocks by the interaction of shallow magmatic systems (Meinert et al., 2003, 2005). Skarn mineralization is the end product of the subduction-related magmatic activities (Burt, 1977; Meinert et al., 2005). The presence of several SCDs (Table 1) and favorable geological setting sweeten the Varzaghan district for further prospecting of skarn Cu mineralization (Karimzadeh Somarin and Moayyed, 2002;
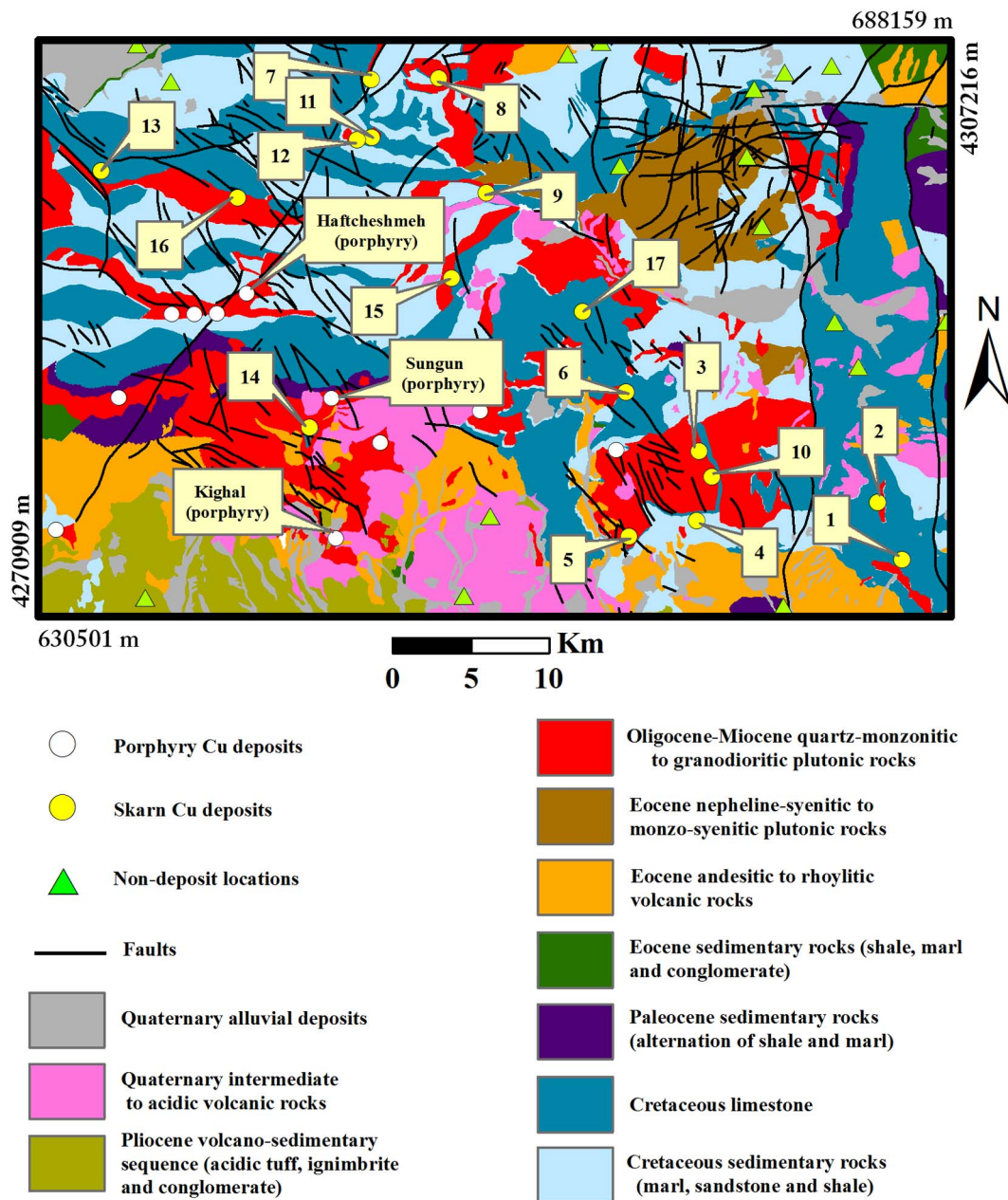
Fig. 2. Generalized geological map of study area and the locations of porphyry and skarn copper deposits (modified after Mehrpartou et al., 1992 and Mehrpartou and Nazer, 1999).

Karimzadeh Somarin, 2004a,b).

The calc-alkaline to alkaline magmatism in late Oligocene caused the development of the SCDs in the study area (Mollai et al., 2009, 2014; Jamali et al., 2010). The emplacement of skarn deposits in the area is restricted to fault zones (Jamali and Mehrabi, 2015) and is spatially associated with the NW-trending faults (Meshkani et al., 2013). The SCDs of the Varzaghan district have been developed at the contacts of the Oligocene-Miocene intrusions and the Cretaceous limestones, and are characterized by the dominant mineral assemblages of chalcopyrite, pyrite, magnetite, sphalerite, galena and epidote (Mollai et al., 2009; Hassanpour, 2013). The Anjerd, Mazraeh and Gowdal deposits are the most important SCDs in the area (Fig. 2 and Table 1). In these deposits, skarnification is developed within or adjacent to the contact of the granitoid intrusions (i.e., endoskarn) and impure carbonates (i.e., exoskarn).

3. Structural controls on skarn Cu mineralization

Structural features, as well as fault systems, control the spatial distribution of the magmatic-related mineral deposits (Cox et al., 1987; Pirajno, 1992). Therefore, the study of the spatial distribution of mineral deposits could provide necessary information for the recognition of structural features controlling the emplacement of mineralization (Kreuzer et al., 2007; Carranza, 2008, 2009a; Carranza et al., 2009; Carranza and Sadeghi, 2010; Lisitsin, 2015). Spatial analyses are beneficial to understand the distribution pattern of mineral deposits. These analyses comprise (1) modeling the spatial distribution of KMDs and (2) measuring the spatial correlation of KMDs with geological features. The former has been performed by the application of the point pattern (Diggle, 1983; Boots and Getis, 1988), fractal (Mandelbrot, 1983) and fry (Fry, 1979) analyses. The above-mentioned analyses could deduce

Table 1
Skarn Cu deposits in the study area.

Id in Fig. 2	Name	Easting	Northing	Mineralization	Heat source and host rock	Magmatism age	References
1	Gowdal (or Gavdel)	47.133	38.600	Cu ± Au	Cretaceous limestone intruded by granodiorite pluton	Oligocene-Miocene	Mollai et al. (2009), Jamali et al. (2010)
2	Agdeh Gheshlagh	47.116	38.633	Cu	Limestone intruded by granodiorite pluton	–	Baniadam (2009)
3	Javansheikh	46.986	38.665	Cu	Alternation of Cretaceous sedimentary rocks intruded by dioritic/granodioritic intrusions	Oligocene-Miocene	Mollai et al. (2009)
4	Zandabad (1)	46.983	38.625	Cu	Cretaceous limestone intruded by granodiorite-monzonite pluton	Oligocene-Miocene	Mollai et al. (2009)
5	Zandabad (2)	46.933	38.616	Cu	Cretaceous limestone intruded by granodiorite-monzonite pluton	Oligocene-Miocene	Mollai et al. (2009)
6	Anjerd	46.933	38.700	Cu + Mo	Cretaceous limestone intruded by granodiorite pluton	Oligocene-Miocene	Mollai et al. (2009, 2014), Hassanpour (2013), Jamali et al. (2010)
7	Abasabad	46.750	38.883	Cu	Limestone intruded by granodiorite pluton	–	Baniadam (2009)
8	Ainalou	46.800	38.883	Cu	Limestone intruded by granodiorite pluton	–	Baniadam (2009)
9	Daghar Daragh (or Gharanigh Daragh)	46.833	38.816	Cu	Cretaceous limestone intruded by granodiorite pluton	Oligocene-Miocene	Mollai et al. (2009)
10	Mazraeh	46.994	38.650	Cu ± Au	Alternation of Cretaceous sedimentary rocks intruded by dioritic/granodioritic intrusions	Oligocene-Miocene	Mollai et al. (2009), Karimzadeh Somarin (2004a,b), Jamali et al. (2010), Mollai et al. (2014)
11	Shabkhaneh	46.750	38.850	Cu	Limestone intruded by granodiorite/monzonite intrusion	–	Baniadam (2009)
12	Mesgar	46.739	38.848	Cu	Limestone intruded by granodiorite/monzonite intrusion	–	Baniadam (2009)
13	Mardan Ghom	46.550	38.833	Cu		–	
14	Sungun (skarn deposit)	46.700	38.683	Cu + Mo + Au	Cretaceous limestone intruded by granodioritic – quartz monzonite pluton	Oligocene-Miocene	Hezarkhani and Williams-Jones (1998), Calagari and Hosseinzadeh (2006), Mollai et al. (2014), Jamali and Mehrabi (2015)
15	Nabijan (skarn deposit)	46.806	38.767	Cu + Au	Cretaceous sedimentary rocks (mainly limestones) intruded by granodioritic – quartz monzonitic intrusion	Oligocene-Miocene	Baniadam (2002, 2009), Jamali et al. (2010)
16	Agha Mira	46.650	38.816	Cu	Limestone intruded by granodiorite pluton	–	Baniadam (2009)
17	Barghzar	46.902	38.747	Cu	Limestone intruded by granodiorite pluton	–	Baniadam (2009)

the quantities and the orientations of structural controls on mineralization (e.g., Carranza, 2009a; Haddad-Martim et al., 2017). The latter has been implemented by the distance distribution analysis (Berman, 1977, 1986) to recognize geological features that are significantly associated with mineral deposits (e.g., Carranza, 2009a; Parsa et al., 2017a). In the following subsections, the implementation of aforementioned spatial analyses is explained.

3.1. Point pattern analysis

In a two-dimensional situation, points can reveal three types of spatial distributions, namely random, clustered and regular (Boots and Getis, 1988). In a random pattern, points lack significant spatial associations and are chaotically distributed. A clustered spatial distribution pattern of mineral deposits, in which the deposits are closer compared with a random pattern, can be representative of the processes that centralize mineralization in certain locations. A regular spatial pattern of mineral deposits in an area, in which the deposits are farther apart compared to a random pattern, indicates the separation of two processes comprising the release of energy and the emplacement of mineralization over the area (Carranza, 2008).

The spatial distribution of mineral deposits is considered to be nonrandom because they have been distributed as a result of underlying geological phenomena (Carranza, 2009a). If a point pattern is nonrandom, it could be resulted as the contribution of either centralizing or spreading processes, both of which could be associated with specific mineralization-related geological settings (Carranza, 2008). Point pattern analysis seeks to prove that the spatial distribution of KMDs is nonrandom. Therefore, the spatial distribution of n KMDs in an under-investigating area should be compared with the spatial distribution of the same number of randomly-distributed points in that area. Therefore, the distances between KMDs are compared with the distances between the randomly-distributed points (Carranza, 2008).

For n points, measured distances from one point to each of the other points are referred to as the 1st-, 2nd-, 3rd- or (n−1)th-order neighbor distances; where the 1st-order neighbor distance is the nearest neighbor distance. Likewise, for n points, there are n−1 means of ordered neighbor distances among individual points; where the mean of the 1st-order neighbor distances is the mean of the nearest neighbor distances among points. If the means of ordered neighbor distances in KMDs are smaller than those in the randomly-distributed points, the spatial distribution of KMDs can be considered as a clustered distribution. On the contrary, if the means of ordered neighbor distances in KMDs are larger than those in the randomly-distributed points, the spatial distribution of KMDs can be considered as a regular distribution. If the means of the ordered neighbor distances in KMDs are similar to those in the randomly-distributed points, the distribution of KMDs can be regarded as random. Consequently, the existence of geological controls of mineralization can be refuted (Carranza, 2009a).

There are 17 SCDs in the study area, for which 16 means of ordered neighbor distances were measured. Likewise, a set of 17 randomly distributed points was generated using the Poisson process (Diggle, 2003; Isham, 2010) within the study area and 16 means of the ordered neighbor distances among these points were calculated as well. The means of the ordered neighbor distances among SCDs are smaller than those of the randomly distributed points (Table 2). Therefore, it could be deduced that the SCDs of the study area tend to have a clustered distribution. Hence, the distribution of the SCDs is not random, and specific processes have contributed in the deposition of SCDs in the study area (cf. Carranza, 2009a).

3.2. Fractal analyses

The box-counting fractal analysis (Mandelbrot, 1983) of mineral deposits has been previously carried out by several researchers (e.g., Kreuzer et al., 2007; Ford and Blenkinsop, 2008; Raines, 2008;

Table 2
Means of different orders of neighbor distances among skarn Cu deposits in the study area.

Order	Neighbor distance	
	Mean of measured distances (km) among the Skarn Cu deposits	Mean of measured distances (km) among the randomly-distributed points
1st	4.888	8.327
2nd	7.750	11.741
3rd	9.043	13.688
4th	10.820	16.516
5th	13.250	18.769
6th	14.744	20.257
7th	17.535	21.929
8th	20.693	23.518
9th	22.988	25.735
10th	25.796	27.739
11th	29.031	29.606
12th	30.691	31.495
13th	31.462	33.784
14th	32.824	36.937
15th	38.050	38.952
16th	43.555	43.042

Carranza, 2008, 2009a). Using this analytical technique, it has been inferred that how many fractal dimensions as the proxies of specific orientations exist in the distribution of mineral deposits. The box-counting fractal analysis involves with the superimposition of grids of different square box sizes (σ) on the map of the spatial distribution of KMDs and counting the number of boxes containing one or more KMDs as $n(\sigma)$. By changing the box sizes (σ), the number of cells containing KMDs, $n(\sigma)$, would change. The relationship between the σ and $n(\sigma)$ is a power-law relationship (e.g., Carranza, 2009a,b), or:

$$n(\sigma) = C\sigma^{-D_b} \qquad (1)$$

where, the D_b and C are the box-counting fractal dimension and a constant, respectively. In a log–log plot the power-law relationship of the Eq. (1) is a linear relationship, or:

$$Logn(\sigma) = LogC - D_b. Log(\sigma) \qquad (2)$$

Hence, the box-counting fractal dimension, D_b, could be estimated from the slopes of straight lines to be fitted to the log–log plot of $n(\sigma)$ versus σ. Whether the spatial distribution of points is random, the box-counting fractal dimension is equal to -2, otherwise it fluctuates within a $(-2, 0)$ range. The number of lines to be fitted to the log–log plot of $n(\sigma)$ versus σ, determines the number of spatial trends in the distribution of mineral deposits and the number of plausible structural controls of mineralization (Carranza, 2009a,b).

The radial-density fractal analysis (Mandelbrot, 1983) of mineral deposits has also been carried out to characterize the spatial distribution of mineralization (Carranza, 2008, 2009a). According to this method, the density of KMDs, d, defined by the number of cells containing KMDs divided by the total number of cells limited by the circles of radius r from KMDs, and the radius, r, have a power-law relationship according to the below equation:

$$d = Cr^{D_R-2} \qquad (3)$$

In the above equation, D_R and C are the radial-density fractal dimension of the KMDs and a constant, respectively. The D_R could be assumed as the slopes of straight lines to be fitted to the log–log plot of density, d, versus the radius, r, or:

$$Logd = LogC + (D_R-2). Log(r) \qquad (4)$$

Carlson (1991) pointed out that the distribution of mineral deposits over an area typically shows two fractal dimensions indicating district- and local-scale controls of mineralization. In this study, similar to several researches (e.g., Carlson, 1991; Cheng and Agterberg, 1995;
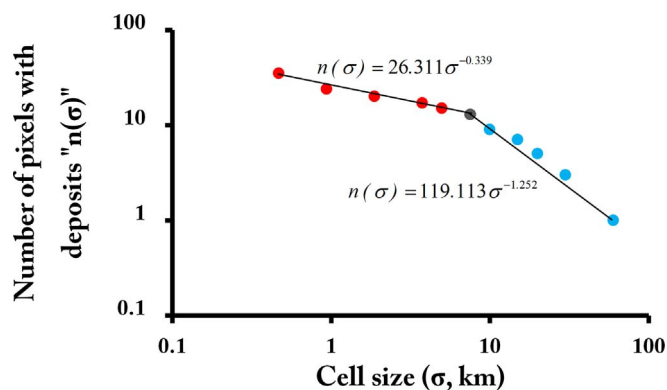
Fig. 3. Log-log plots of σ versus n (σ) manifesting two spatial patterns of the skarn copper deposits in the study area.

Cheng et al., 1996; Raines, 2008; Zuo et al., 2009), two straight lines have been fitted to the log–log plot of $n(\sigma)$ versus σ (Fig. 3). The fitted straight lines (Fig. 3) are optimum because the addition or reduction of any other straight lines would either lower the regression coefficients or raise the minimum squared errors of the lines (Cheng et al., 2010). These results suggest that the distribution of the SCDs in the area is not random (cf. Raines, 2008; Carranza, 2009a) and specifically is bifractal. In the Fig. 3, the left straight line with the D_b value of -0.399 and the σ values of ≤ 7.5 km is responsible for local-scale geological processes of mineral deposition. The right straight line with the D_b value of -1.252 and the σ values of > 7.5 km is related to the district-scale geological processes of the deposit distribution in the area (cf. Carranza, 2008, 2009a).

To estimate the radial-density fractal dimensions of the spatial distribution of the SCDs in the Varzaghan district, the distribution map of the SCDs was converted to a 100 m × 100 m cell size raster-based map, in which each SCD was located in a single cell. Then, the d values of the SCDs were calculated based on different circles portrayed by different radiuses centered at the SCDs. The plot of log (d) versus log (r), shows two optimum (cf. Cheng et al., 2010) radial-density fractal dimensions (Fig. 4). Thus, it could be deduced that the distribution of SCDs at district-scale is non-random and two geological processes operated in the distribution of the SCDs at different scales (cf. Carranza, 2009a). Similar to the results of the box-counting fractal analysis (Fig. 3), the left line in Fig. 4 is responsible for the local-scale geological processes that influenced in the distribution of the SCDs at the distances of below 7.5 km. Likewise, the right line in this figure is representative of the district-scale geological processes that operated in the distribution of the SCDs at distances of beyond 7.5 km (cf. Carranza, 2009a).

The results of two fractal analyses (Figs. 3 and 4) have conformity, both of which suggest the bi-fractality and non-randomness of the
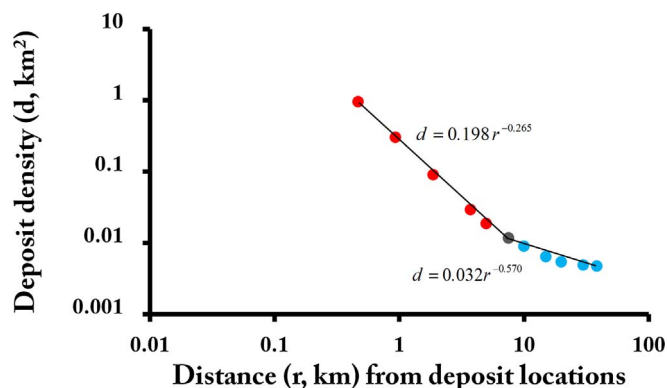

Fig. 4. Log-log plots of distances from individual skarn copper deposits versus the deposit densities manifesting two individual spatial patterns.

distribution of the SCDs. Accordingly, as pointed out by Carlson (1991), Raines (2008) and Carranza (2009a), below and beyond 7.5 km distances from the deposit locations, two processes have incorporated in the distribution of the SCDs in the study area. The former and the latter respectively describe the local- and the district-scale geological processes that operated in the skarn mineral deposition.

3.3. Fry analysis

Fry analysis (Fry, 1979) can be applied to characterize the spatial distribution of mineral deposits, through which the orientations of plausible controls of mineralization have been investigated (e.g., Vearncombe and Vearncombe, 1999; Carranza, 2008, 2009a; Kreuzer et al., 2007; Lisitsin, 2015; Haddad-Martim et al., 2017). In this method, for n KMDs that are considered as points, $n^2 - n$ translated points are delivered. Therefore, this analysis can enhance the subtle patterns of the spatial distribution of KMDs. Details of this method could be found in related publications (e.g., Fry, 1979; Vearncombe and Vearncombe, 1999; Carranza, 2009a). By measuring the orientations and distances between the pairs of translated points, rose diagrams could be constructed from which the inconspicuous controlling processes of mineralization could be reflected. Rose diagrams could be plotted for (a) all of the translated points and (b) the translated points that are located within specific distances. The former case represents the orientations and numbers of geological processes that contribute to the mineral deposition at the district-scale, while the latter case could be used to provide information on the local-scale mineralization processes (Carranza, 2009a; Haddad-Martim et al., 2017).

Based on the original locations of 17 SCDs in the area, 272 translated points were delivered. Following Carranza (2009a), the translated points were centered at the original deposit locations, for better interpretations (Fig. 5a). The rose diagram of all pairs of translated points was constructed (Fig. 5b), which suggests a major 110°–150° or 290°–330° orientation, manifesting an NW-trending structural control on mineralization at district-scale (cf. Carranza, 2008, 2009a). The rose diagram of the pairs of translated points with the distances of below 7.5 km was further constructed (Fig. 5b), suggesting a 150°–180° or 330°–360° (N-S) trending structural control on mineralization at local-scale (cf. Carranza, 2008, 2009a). These results of the fry analysis not only cohere with those of fractal analyses but also suggest that the local- and district-scale structural controls of skarn mineralization have N-S and NW-SE orientations, respectively.

3.4. Spatial association of structural features with skarn Cu deposits

Different structural features with diverse orientations are the outcomes of various geological processes (Faulkner et al., 2010), few of which might be associated with mineralization (Carranza, 2008). Different faults of the study area were grouped according to their specific orientations. The degree of their spatial association with mineralization was further assessed by distance distribution analysis (Berman, 1977, 1986). This technique has been applied for measuring the degree of the spatial association of a set of geological features with mineral deposits (e.g., Carranza, 2009a; Parsa et al., 2017a). Two curves are simultaneously constructed in the distance distribution analysis, namely, the cumulative relative frequency distribution of the distances from every location to a set of geological features (C_e) and the cumulative relative frequency distribution of distances from the locations of KMDs to the same set of geological features (C_d). The former curve denotes an entirely random pattern, while the latter curve might represent underlying geological processes that contribute to the mineral deposition. An additional curve, which manifests the difference of the above-mentioned curves ($d = C_{d} - C_e$) denotes the quantity of the spatial association of the mineral deposits with geological features. The values $d > 0$ and < 0 show positive and negative spatial association between the KMDs and geological features, respectively. In this regard, the
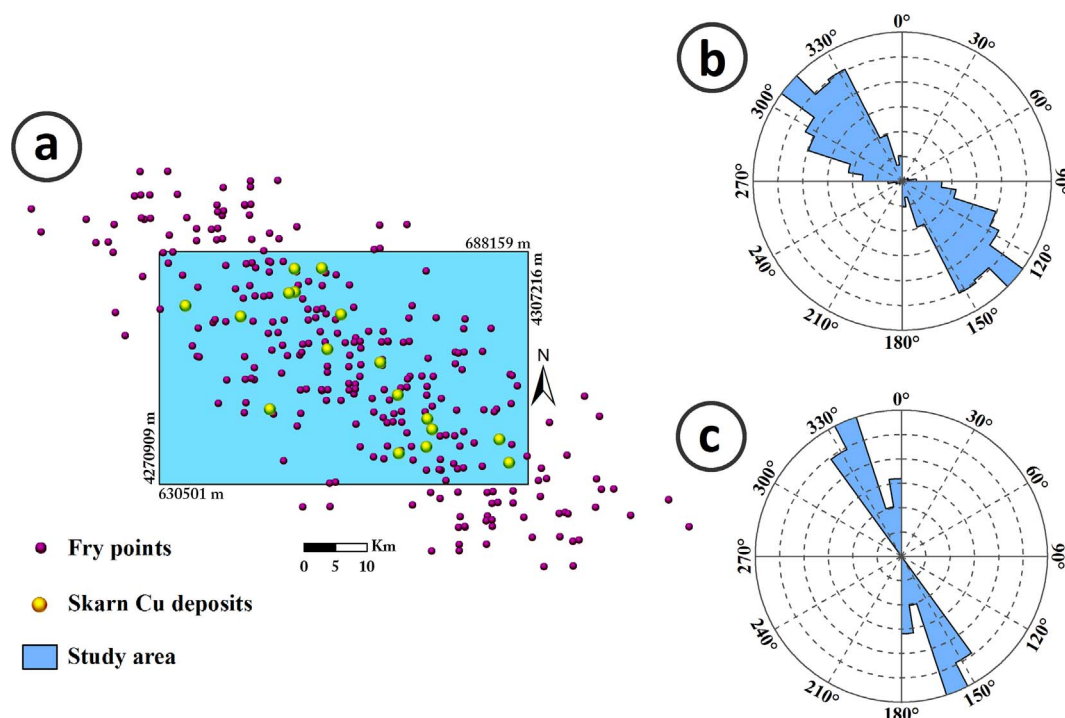
Fig. 5. (a) Fry points of the skarn copper deposits in the study area, (b) rose diagram of trends based on all pairs of fry points and (c) rose diagram of trends based on points < 7.5 km distances of each other.

maximum value of the *d* reflects a distance that shows the most significant spatial association between geological features and mineral deposits (Carranza, 2009a).

In the study area, beyond 12 km distances of the northern-trending faults, there are poor spatial associations with the SCDs (Fig. 6a). Likewise, beyond 16 km distances of the E-W trending faults, there are weak positive spatial associations with the SCDs (Fig. 6b). Therefore, the spatial associations of the N-S and E-W trending faults with the SCDs are not significant. Similarly, there are no significant spatial correlations between the NE-trending faults and the SCDs (Fig. 6c). However, significant positive spatial associations exist between the NW-trending faults and the SCDs (Fig. 6d). Within 1 km distances of the NW-trending faults, the most significant spatial correlation with the SCDs is observed (Fig. 6d). Around 80% of the SCDs are distributed within the areas of below 1 km distances to the NW-trending faults (Fig. 6d).

3.5. Eliciting the structural controls on mineralization

According to the results of point pattern analysis, the distribution of SCDs in the study area is nonrandom and specifically shows a clustered pattern (Table 2). This is reasonable because these deposits are confined to the boundaries of Oligocene-Miocene intrusive rocks (Karimzadeh Somarin and Moayyed, 2002; Mollai et al., 2009), that supports a clustered distribution. The results of fractal analyses suggest the bi-fractal distribution of the SCDs (Figs. 3 and 4). Therefore, according to the studies of Carlson (1991) and Carranza (2009a), two geological processes that operated in the distribution of the SCDs at distances of ≤7.5 km and > 7.5 km could be deduced from fractal analyses (Figs. 3 and 4). The results of fry analysis suggest that the distribution of the SCDs at the distances ≤7.5 km follow an N-S trend manifesting local-scale controls of skarn mineralization (Fig. 5c). These results are significant because local studies on the SCDs of the Varzaghan district recommended the N-S trending faults to be directly associated with the skarnification (e.g., Mollai et al., 2009; Jamali et al., 2010; Mokhtari et al., 2017). Fry analysis also revealed that the district-scale (i.e., distances > 7.5 km) geological processes, which yielded in the

distribution of the SCDs in the Varzaghan district, follow an NW-SE trend (Fig. 5a and b). Such results are meaningful because the NW-trending faults were previously manifested to be spatially associated with the skarn copper mineralization of the Varzaghan district (Meshkani et al., 2013). Overall, the synthesis of the results of point pattern, fractal and fry analyses with those of the distance distribution analysis (Fig. 6) suggest the NW-SE trending faults as plausible district-scale structural controls on skarn Cu mineralization.

4. Lithological controls on skarn Cu mineralization

The spatial distributions of the SCDs in the Varzaghan district are confined to the areas where the Oligocene-Miocene plutonic rocks intruded the Cretaceous limestones (Mollai et al., 2009). The generic characteristics of 17 known SCDs of the Varzaghan district support that the Oligocene-Miocene plutonic rocks and the Cretaceous limestones are heat sources and host rocks of skarn Cu mineralization, respectively (Karimzadeh Somarin, 2004a,b; Mollai et al., 2009). Therefore, the distance distribution analysis was conducted to quantify the spatial association of the SCDs with contacts of the Oligocene-Miocene plutonic rocks and contacts of the Cretaceous limestones.

There are strong positive spatial associations between the SCDs and the contacts of the Oligocene-Miocene intrusive rocks (Fig. 7a). However, there are weak positive spatial associations between the Cretaceous limestones and SCDs (Fig. 7b). That is because few of the Cretaceous limestones, which are exposed in the majority of the study area, are in contact with the Oligocene-Miocene intrusive rocks. Thus, the Oligocene-Miocene intrusive rocks can be used as a significant lithological evidence of skarn Cu mineralization in the study area.

5. Significant geochemical signatures of skarn Cu deposits

Recognition of significant geochemical signatures of mineral deposits of the targeted type is effective in the calibration of exploration criteria, and consequently in the delineation of reliable exploration targets (e.g., Mokhtari et al., 2014; Parsa et al., 2016a–c, 2017a–e; Yousefi et al., 2014; Yousefi, 2017). For this, multivariate geochemical
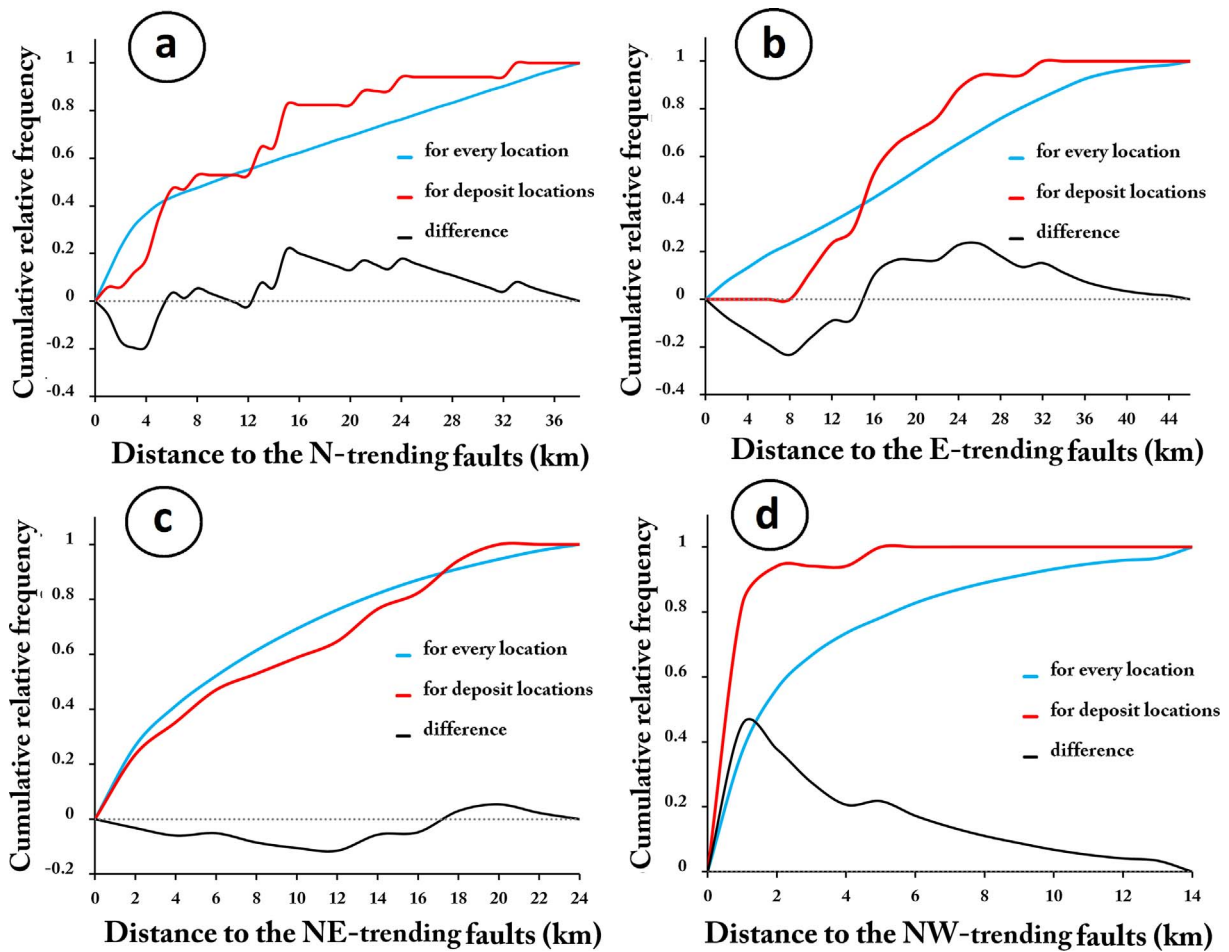
Fig. 6. Plots showing distances from every location and from deposit locations to (a) N-S trending, (b) E-W trending, (c) NE-SW trending and (d) NW-SE trending faults.

analyses can be applied in conjunction with spatial analysis of geochemical signatures with mineral deposits (Parsa et al., 2016a). In this study, the robust factor analysis (RFA) of compositional data (Filzmoser et al., 2009) was applied in conjunction with the distance distribution analysis (Berman, 1977, 1986) to derive significant multi-element geochemical signatures of the SCDs. The RFA that has been applied for the recognition of mineralization-related element associations (e.g., Parsa et al., 2017c) is the robustified version (Pison et al., 2003) of the exploratory factor analysis (Treiblmaier and Filzmoser, 2010) through which the shortcomings of FA has been modulated (Filzmoser et al.,

2009). Details about the RFA could be found in Filzmoser et al. (2009).

There are 913 stream sediment samples, collected from the study area by the Geological Survey of Iran. The collected samples were analyzed for multi-elements (Cu, Mo, Ag, Pb, Zn, As, Sb, Pb, Bi and Zn) by inductively coupled plasma optical emission spectrometer. The detection limits of the examined elements were: 0.5 ppm for As; 0.2 ppm for Pb, Zn and Cu; 0.1 ppm for Mo, Bi and Sb and 0.01 ppm for Ag. Fire assay method was further employed for preconcentration of gold, and the final solution was measured by the atomic absorption spectrophotometry with a detection limit of 1 ppb. The method of Thompson
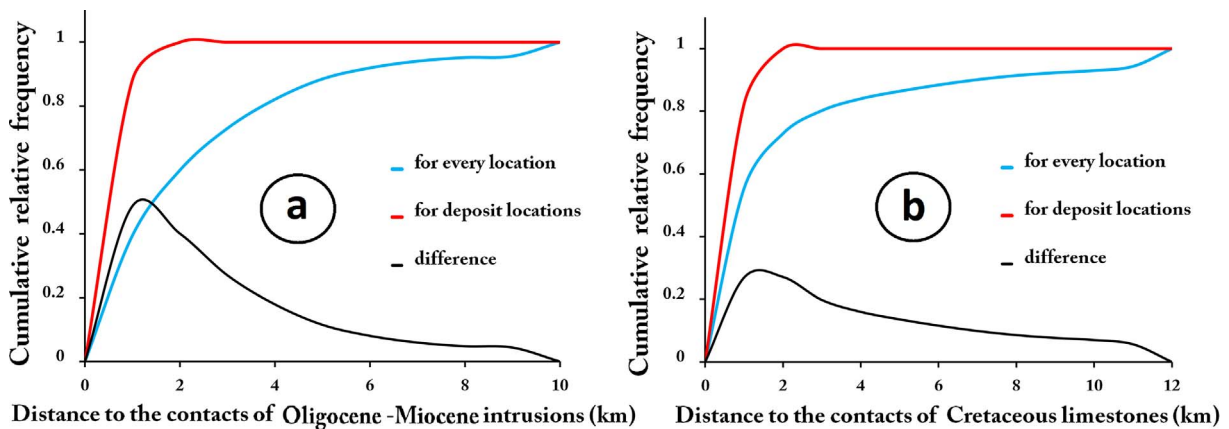

Fig. 7. Plots showing distances from every location and from deposit locations to (a) contacts of Oligocene-Miocene intrusions and (b) contacts of the Cretaceous carbonate sedimentary rocks.

and Howarth (1976) was then employed for assessing the analytical precision of individual elements. Results revealed that the analytical precision of all of the analyzed elements was better than 10% at the 95% of confidence level.

The isometric log-ratio transformation (ilr: Egozcue et al., 2003) was applied on the raw-data of 11 analyzed elements. The initial covariance matrix of the variables was estimated based on the ilr-transformed data. Since the ilr-transformation yielded in the scarification of one of the variables (Egozcue et al., 2003), the resulting covariance matrix was back-transformed to the centered log-ratio (clr: Aitchison, 1986) space, in which interpretation of the results of RFA is possible (Filzmoser et al., 2009). The number of the derived factors was set to be three because these factors not only explain 85.9% of the total variability but also they have precisely discriminated the elemental associations (e.g., Filzmoser et al., 2009). The principle factor analysis (Reimann et al., 2002), the varimax rotation (Kaiser, 1958) and the Bartlett method (Reimann et al., 2002) were used as the methods of deriving the factors, rotating the factor loadings and deriving the factor scores, respectively. Significant loadings were retained based on the absolute threshold value of 0.4, as this value can be applied in the precise interpretation of factors (Filzmoser et al., 2009; Treiblmaier and Filzmoser, 2010).

The first robust factor explains 48.9% of total variability and represents the contribution of As, Sb and Zn with negative loadings (Table 3), while it is representative of an Au-Ag-Cu-Mo-Bi element association with positive loadings (Table 3). The second factor, which explains 26.8% of the total variability, represents the significant contribution of As and Sb with negative loadings and the significant contribution of Zn with positive loading (Table 3). The biplots of the robust factor 1 versus the robust factor 2 explicitly demonstrates the association of Au, Ag, Cu, Mo and Bi (Fig. 8). The third factor with the least contribution in the total variability (i.e., 10.2%) manifests a Pb-Zn element association (Table 3). According to the factor loadings (Table 3) and biplots (Fig. 8), the first factor could be representative of skarn copper mineralization within the Varzaghan district. The elements contributed in factor 1 are indicators of, and have been used to, investigate skarn copper mineralization (e.g., Meinert, 1992).

In order to model the spatial distribution of geochemical anomalies, the factor score values of each stream sediment sample were specified to their corresponding catchment basins. This is because the element concentration of each stream sediment sample is representative of its upstream materials (Bonham-Carter and Goodfellow, 1984, 1986; Spadoni et al., 2005; Spadoni, 2006; Carranza, 2008, 2010). Besides, catchment basin modeling of geochemical anomalies, compared to the interpolation methods, yields in the enhanced delineation of geochemical anomalies through stream sediment sampling schemes (Carranza, 2010; Yousefi et al., 2013; Parsa et al., 2016a).

To further explore the significance of the derived factors in the description of the SCDs in the study area, cumulative decreasing distance distribution analysis (e.g., Carranza, 2009a) was conducted to
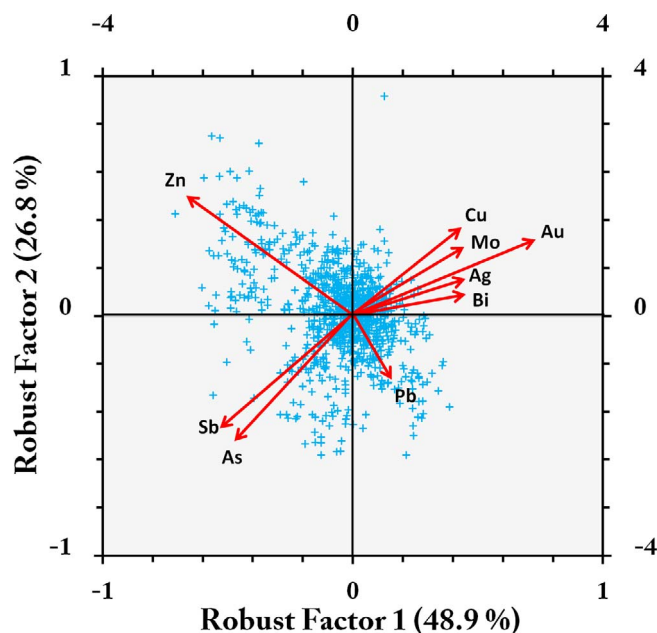

Fig. 8. Biplots of robust factor 1 versus robust factor 2 of geochemical variables.

recognize whether the robust factors are significant geochemical signatures of the skarn Cu mineralization. Factor 1 demonstrates a remarkable positive spatial association with the SCDs (Fig. 9a). Around 60% of the SCDs are located in areas where the scores of factor 1 are higher than -0.38 (Fig. 9a). There are no significant or remarkable positive spatial coincidences between the scores of factor 2 and 3 and the SCDs (Fig. 9b and c). Therefore, it is suggested that the multi-element geochemical association of Au, Ag, Cu, Mo and Bi in – stream sediment data of the Varzaghan district (i.e., the robust factor 1: Fig. 8 and Table 3) is an efficient geochemical signature for vectoring toward skarn mineralized zones.

6. Data-driven modeling of the skarn Cu prospectivity

In order to delineate further exploration targets of the SCDs in the study area, two data-driven modeling process of mineral prospectivity, namely the random forest algorithm (RF: Breiman, 2001) and the logistic regression (LR: Hosmer and Lemeshow, 2000) were conducted. Both of the modeling methods (a) are robust and do not require the input data set to follow a specific distribution; (b) do not require the input variables to be conditionally independent; (c) can model the probability of the occurrence of a dichotomous target variable based on a set of continuous or categorical predictor variables; (d) are multivariate approaches that consider the complexities of geological processes and (e) have been successfully applied to model the mineral prospectivity of various terrains (e.g., Chung and Agterberg, 1980; Carranza et al., 2008; Rodriguez-Galiano et al., 2015; Carranza and Laborte, 2015a,b, 2016).

Target variable of the two prospectivity mapping approaches is modeled as a set of event and non-event points. These points are the deposit (values = 1) and non-deposit (values = 0) locations, respectively. These locations should be defined by considering the following criteria (Nykänen et al., 2015; Carranza and Laborte, 2016):

- The number of the non-deposit locations (hereinafter denoted as NDLs) should be equal to that of the deposit locations, which is 17 in this study.
- NDLs should be far from the deposit locations so that their geochemical and geological characteristics would be different from the deposits. To this end, the point pattern analysis was implemented to recognize the maximum distance from the KMDs, in which there is a

Table 3
Rotated component matrix of robust factor analysis. Significant loadings (bolded values) are selected based on the absolute threshold value of 0.4.

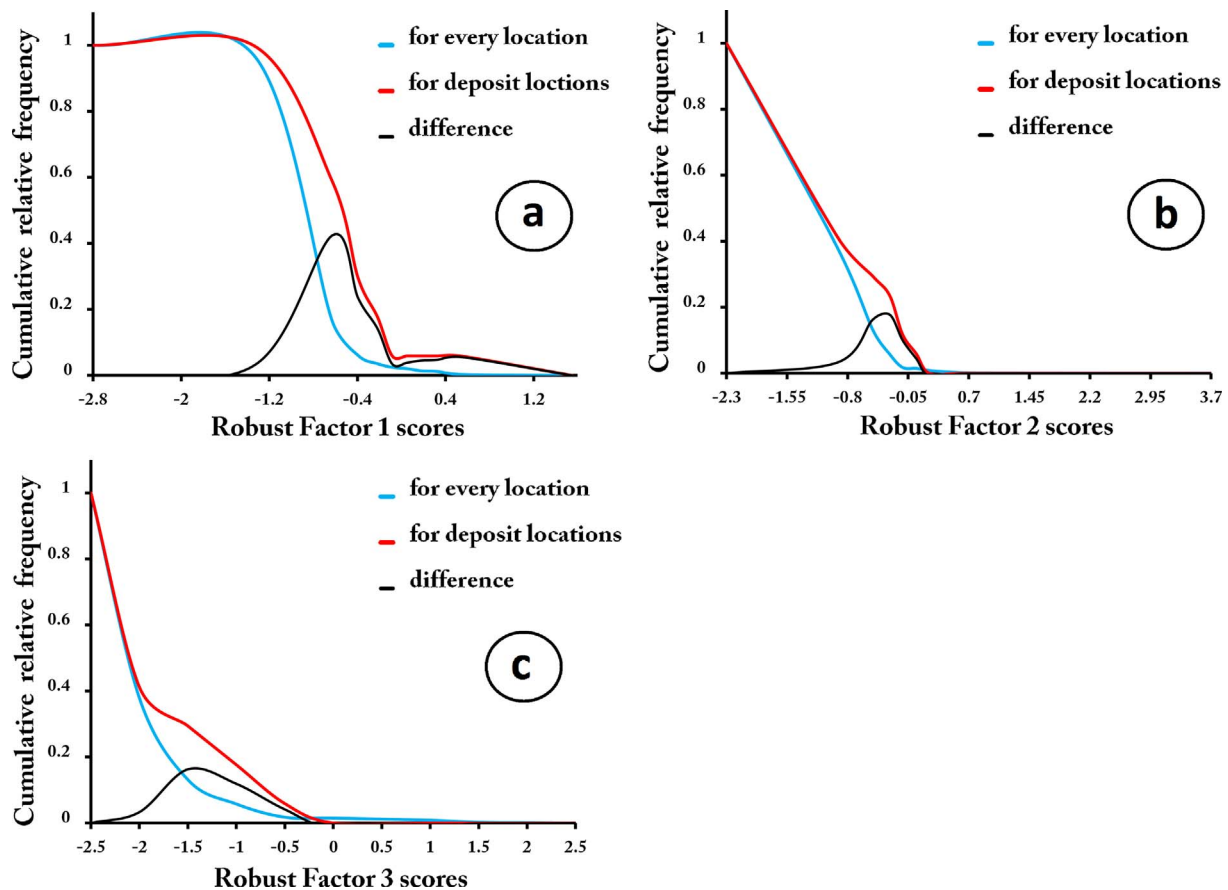| Element	Factor1	Factor2	Factor 3
As	−0.418	−0.524	0.110
Sb	−0.523	−0.480	0.125
Zn	−0.644	0.474	0.567
Cu	0.485	0.355	−0.105
Mo	0.488	0.228	−0.226
Bi	0.479	0.149	−0.168
Pb	0.210	−0.290	0.620
Au	0.638	0.249	−0.341
Ag	0.458	0.199	−0.257
Var.	48.9	26.8	10.2
Cum. Var.	48.9	75.7	85.9

Fig. 9. Plots showing difference between robust factor scores at each cells and cells containing SCDs (a) robust factor 1, (b) robust factor 2 and (c) robust factor 3.

100% probability of finding a deposit. This distance was found to be 7 km, which leaves 45% of the study area for NDLs.

- Unlike the SCDs that have a clustered spatial distribution (Table 2), NDLs should be chaotically distributed. Therefore, point pattern analysis was conducted to generate 17 random points in the remaining 45% of the study area (Fig. 10).

A set of target variables that was used in both modeling methods was generated according to the procedure outlined above. District-scale controls on mineralization (Sections 3 and 4) and the significant multi-element geochemical signature of the SCDs (Section 5) were translated to a set of predictor variables or evidence layers to be used in the modeling methods. These predictor variables were continuously generated so that systematic uncertainties of MPM, resulting from improper classification of geological data, could be reduced (Yousefi and Carranza, 2015a,b, 2016). Following a procedure outlined by Carranza (2009b), a unit pixel size of 100 m × 100 m was objectively selected for generation of evidence layers and the upcoming processes of MPM. Fig. 10 depicts the exploration evidence layers generated.

6.1. Logistic regression modeling

The LR models the logit of the probability of the occurrence of mineralization, as a binary target variable, Y, based on a set of evidence layers or predictor variables, X_i, using a nonlinear relationship, according to the following equation (Hosmer and Lemeshow, 2000):

$$Logit(P) = \ln\left(\frac{P}{1-P}\right) = \beta_0 + \beta_1 . X_1 + \beta_2 . X_2 + ... + \beta_n . X_n \quad (5)$$

where $Logit(P)$ is the logit of the probability of the occurrence of the target variable, β_0 is the intercept of the model and $\beta_1, \beta_2, ... , \beta_i$ are the

slopes of predictor variables in the LR model. The probability of the occurrence of the target variable, P, then could be derived via the Eq. (6):

$$P = \frac{1}{1 + e^{-Logit(P)}} \quad (6)$$

In this study, the backward stepwise procedure was used for optimizing the predictor variables in the final LR model (e.g., Carranza et al., 2008). The values of $(\beta_0, \beta_1, ... , \beta_i)$ were determined by the maximum likelihood method (Cox and Snell, 1989). The Wald statistic was used for assessing the significance of the incorporation of predictor variables within the LR model (Menard, 2001). Besides, a 95% of confidence level was used for retaining significant predictor variables, based on which the predictor variables whose significance levels are lower than 0.05 have effectively contributed in the final LR model (e.g., Mokhtari, 2014). The final LR model demonstrates that all the evidence layers are significantly incorporated in the model (Table 4). Such results are reliable because all the three evidence layers are efficient exploration criteria that were selected through investigations of controls on mineralization. Fig. 11 shows the prospectivity model generated by the LR method.

6.2. Random forest modeling

The RF is an ensemble of multiple decision trees (DTs: Breiman, 1984) that could be utilized in regression and classification problems (Breiman, 2001). Each DT uses a random subset of training samples which are taken with replacement from the original data (Breiman, 1996). About two-thirds of samples are used for generation of models, while the rest of them that are called out-of-bag (OOB) samples are used for validation of the results using the OOB error. RF initiates with the purification of child nodes through splitting the target variable based
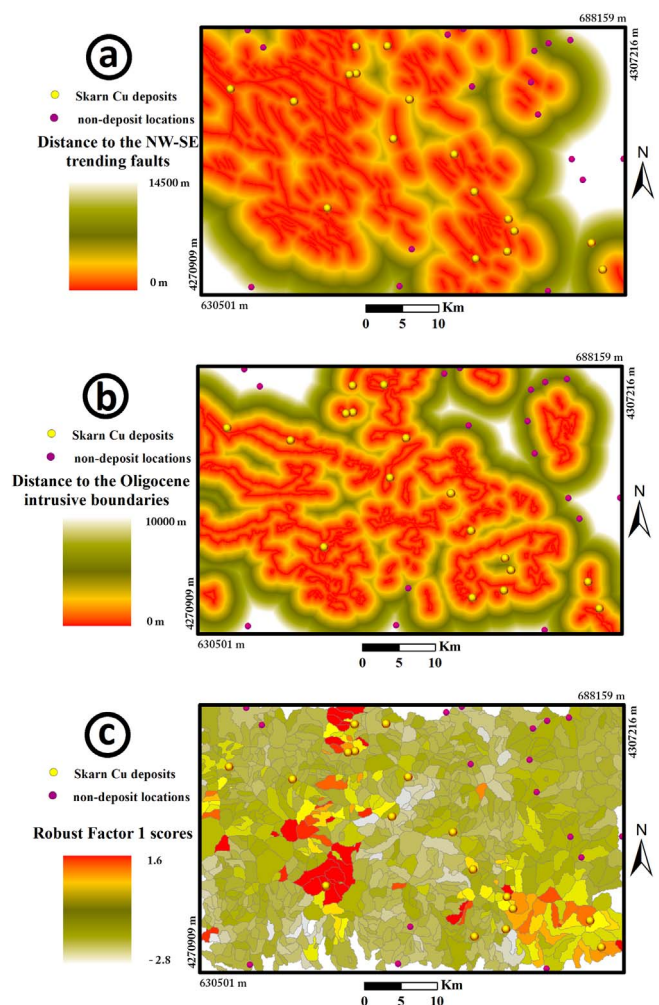
Fig. 10. Three evidence layers generated, namely: (a) Distance to NW-SE trending faults, (b) Distance to Oligocene-Miocene intrusion boundaries and (c) robust factor 1 scores specified to sample catchment basins.

Table 4
Coefficients (βi) of predictor variables of final LR model.

Predictors	Coefficient (βi)	Wald statistics	Significance
Distance to the NW-trending faults	49.125	10.276	.001
Distance to the Oligocene-Miocene intrusive rocks	53.112	11.716	.001
Robust geochemical Factor 1 scores	31.139	4.767	.029
Intercept (β₀)	−44.040	10.789	.001

on predictor variables from the parent node. The splitting successively iterates until a pre-defined stop criterion is reached. Through this process, every DT has reached to its simple regression or classification model. RF then averages the results of various DTs to gain the final model. More descriptions about the RF algorithm could be found in Breiman (2001).

In this study, the 'randomForest' package (Liaw and Wiener, 2002) of the R statistical freeware (R development core team, 2008) was used for RF modeling. Two parameters should be tuned prior to the RF analysis, namely the number of trees to be grown and the number of predictors to be entered at each node. Picking a large number of trees results in stable predictions (Micheletti et al., 2014), and therefore 20,000 trees were selected (e.g., Carranza and Laborte, 2016). Besides,
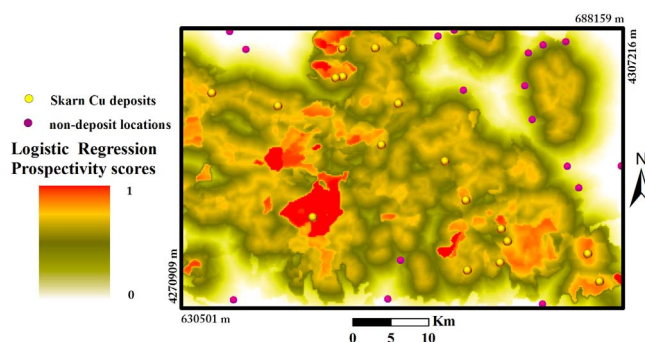

Fig. 11. Mineral prospectivity scores generated by the LR method.

Table 5
The accuracy of RF modeling inferred from OOB error rate and confusion matrix of prediction.

Error for the classification of the deposit locations	(0 out of 17 incorrect prediction) 0%
Error for the classification of the non-deposit locations	(1 out of 17 incorrect prediction) 0.058%
OOB error	2.94%
Model accuracy	97.06%

the optimum number of predictor variables to be entered at each node was objectively selected by the 'tuneRF' function of the 'randomForest' package (Liaw and Wiener, 2002), which yielded in the minimizing of the OOB error (e.g., Pourghasemi and Kerle, 2016; Carranza and Laborte, 2016).

The OOB error was used for the evaluation of the performance of the RF model. The OOB error was 2.94%, and therefore the model accuracy is 97.06% (Table 5), which indicates that the model is somehow perfect (cf. Breiman, 2001). Since the prospectivity scores derived by the RF modeling are probability values ranging from 0 to 1, the prospectivity values of ≥0.5 are considered as prospective for the deposit-type sought and vice versa (Carranza and Laborte, 2016). According to the mentioned criterion, a confusion matrix was generated and revealed that the RF modeling resulted in the classification accuracy of 100% for deposit locations and the classification error of 0.058% for NDLs (Table 5).

The importance of predictor variables in the RF model could be further assessed via the mean decrease in accuracy and the mean decrease in node impurity or the Gini impurity index (Breiman, 2001). The former is determined during the calculation of the OOB error, while the latter is a measure of how each variable contributes to the homogeneity of the nodes and the final RF model. The higher the mean decrease accuracy and the higher the Gini impurity index of a predictor are, the more important the predictor would be (Breiman, 2001). Fig. 12 depicts the two above-mentioned criteria measured for the predictor variables. According to this figure, the most important predictor contributing in the final RF model is the distance to the Oligocene-Miocene intrusive rocks, while the robust factor 1 of compositional geochemical data is the least significant predictor contributing in the final RF model. Fig. 13 shows the final RF model of the skarn Cu prospectivity in the study area.

6.3. Comparison of models

The visual comparison of the two prospectivity models generated manifests that these models are completely different (Figs. 11 and 13). Quantitative comparison of the models was further implemented using success- (Agterberg and Bonham-Carter, 2005) and prediction-rate (Chung and Fabbri, 2003) curves. The former denotes how well the results correlate with the training samples (Agterberg and Bonham-Carter, 2005), while the latter reveals the chance of finding
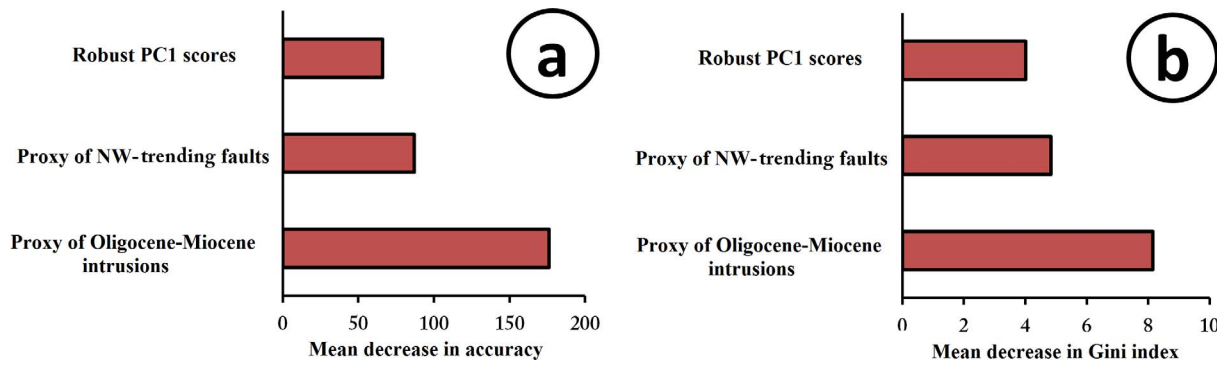
Fig. 12. Measures of predictor variable importance derived by RF method: (a) mean decrease in accuracy and (b) mean decrease in Gini impurity index.
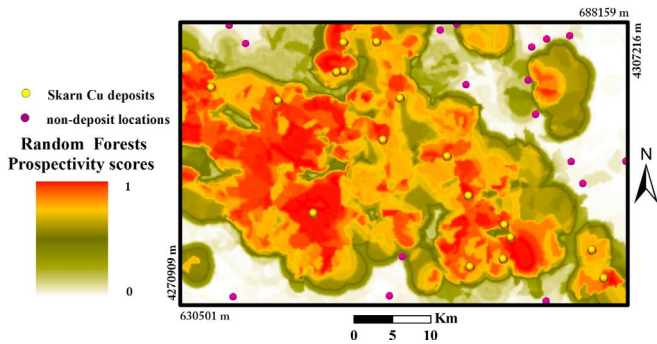

Fig. 13. Mineral prospectivity scores generated by RF method.

undiscovered deposits by the models (Chung and Fabbri, 2003). For the generation of success-rate curves, according to Agterberg and Bonham-Carter (2005), the prospectivity scores of the models have undergone a series of discretization processes based on the cut-off values at the five percentile intervals. Based on each of the cut-off values two parameters comprising (a) the portion of the area enclosed by the pattern representing the delimited prospectivity zone, P_a, and (b) the portion of mineral deposits delimited in the prospectivity zone, P_d, were calculated. The values of P_a and P_d for different threshold values were estimated and then plotted in the vertical and horizontal axes, respectively.

For the construction of the prediction-rate curves, the leave-one-out approach (Fabbri and Chung, 2008) was applied. In this approach, as Fabbri and Chung (2008) mentioned one KMD is excluded from a set of m KMDs, and the remaining m-1 KMDs are used for generating a prospectivity model. Then the generated prospectivity model is cross-validated with the excluded KMD. This procedure iterates m times, each time with excluding a different KMD for cross-validating. The values of mineral prospectivity models at each excluded KMD are used as thresholds for classification of mineral prospectivity scores. The proportion of delimited prospectivity areas by the m threshold values in the m generated prospectivity models are sorted increasingly. Then, the cumulative increasing proportion of areas, P_a, and the cumulative increasing proportion of the KMDs, P_d, are derived. Similar to the success-rate curves, prediction-rate curves are constructed by using P_a values on the horizontal axis versus P_d values on the vertical axis. The success-rate curve of the RF model lies above that of the LR model (Fig. 14a), representing that the former compared with the latter possesses a stronger association between the target and predictor variables.

The prediction-rate curves of both models lie below their corresponding success-rate curves (Fig. 14a and b). Such results are expected because if a model is correctly generated its success-rate would be better than its prediction-rate (Chung and Fabbri, 2003). The prediction-rate curve of the RF model lies above that of the LR model (Fig. 14b), manifesting that the former model (Fig. 13) compared to the latter model (Fig. 11) has a stronger reliability for finding undiscovered skarn Cu deposits in the study area.
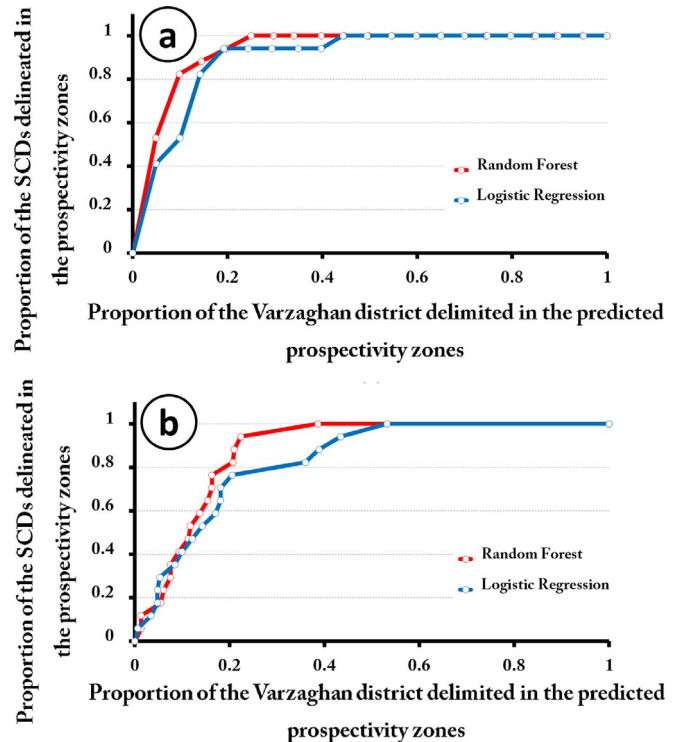

Fig. 14. Success-rate (a) and prediction-rate (b) curves of mineral prospectivity models generated.

6.4. Exploration targets

Raster maps of mineral prospectivity should be classified for interpretation purposes (Asadi et al., 2015; Carranza and Laborte, 2016; Parsa et al., 2016a,b). For this, the plots of cumulative areas versus cumulative prospectivity scores (Porwal et al., 2003) were generated (Fig. 15). In these plots, sudden changes in the slope of fitted curves manifest the possible threshold values through which the continuous maps could be classified. A threshold was derived for each of the prospectivity models according to the plots of Fig. 15. Consequently, two binary maps showing the delineated exploration targets were generated (Fig. 16). The target areas of the LR model (Fig. 16a) have occupied 19.23% of the study area, in which 76.42% of the SCDs are delineated. However, the target areas of the RF model (Fig. 16b) have occupied 17.64% of the study area, in which all the SCDs are delineated. Therefore, it could be deduced that the target areas generated by the RF model are more reliable than those generated by the LR model.

In addition to the results of table 5 in the accuracy assessment of the RF model and the success- and prediction-rate curves, field operations demonstrated that the delineated exploration targets of the RF model
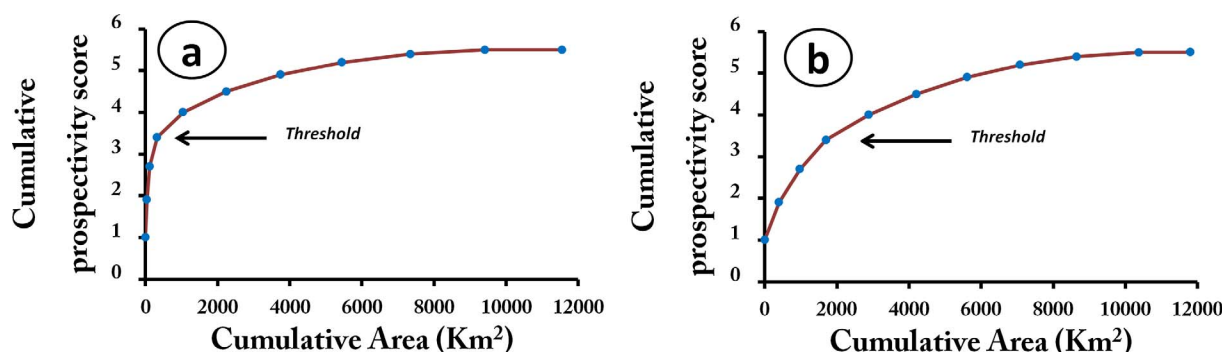
Fig. 15. Plots showing the cumulative area versus cumulative prospectivity scores for deriving thresholds to discretize prospectivity models: (a) for LR model and (b) for RF model.

are much more robust than that of LR model. Field surveys revealed that there are pieces of evidence of skarn copper mineralization within the target zones. Fig. 17 demonstrates a granodiorite stock intruded into Cretaceous limestones, which yielded in the development of endoskarn and exoskarn zones. The dominant mineral assemblage in the observed outcrops of skarn zones includes chalcopyrite, pyrite and magnetite as ore minerals and quartz, calcite, garnet and epidote as the main gangue minerals (Fig. 17b and c and Fig. 18). Malachite and azurite of the secondary origin were also found in the observed exoskarn zones. Therefore, based on the results of statistical analyses and initial field surveys, it is worthy to follow up further exploration within the delineated target zones of the RF model.

7. Discussion and conclusion

Systematic uncertainties of mineral prospectivity models could be reduced by the proper selection of exploration criteria (Carranza, 2008; Yousefi and Carranza, 2015a,b; Andrada de Palomera et al., 2015; Lindsay et al., 2016; Parsa et al., 2017a). To achieve this goal, recognizing significant geochemical signatures of the deposit of the targeted type (Parsa et al., 2016a,b) and translation of geological controls on ore deposition (Carranza, 2008, 2009a) into indicator evidence layers are essential. Analyses of the spatial distribution of known mineral deposits in an area and quantifying their spatial association with evidential features are beneficial to understand the plausible controls on ore deposition, and consequently, to develop calibrated exploration criteria (e.g., Kreuzer et al., 2007; Carranza, 2008, 2009a; Lisitsin, 2015). According to the results of spatial analyses conducted in this paper, the following exploration criteria were elicited for vectoring toward skarn copper mineralized zones in the study area:

- The Oligocene-Miocene granitoid intrusions served as the heat

source of the skarn copper mineralization of the Varzaghan district. These results are consistent with the former reports of Karimzadeh Somarin and Moayyed (2002), Mollai et al. (2009) and Jamali et al. (2010), which concluded that the late Oligocene-Miocene fertile plutons are responsible for deposition of the skarn copper ore in the Varzaghan district.

- Most of the skarn-type Cu deposits of the study area are distributed in peripheral to the areas with little distances to the NW-trending faults. Therefore, the NW-trending faults are the district-scale structural controls on the skarn mineralization. Such results are consistent with the previous findings of Meshkani et al. (2013) and Jamali et al. (2010).

- Relative enrichment of Cu, Mo, Au, Ag and Bi in the stream sediment samples, are significant geochemical signatures of the skarn Cu mineralization in the Varzaghan district. In this study, the robust factor 1 (Fig. 8) is a multi-element geochemical signature manifesting the enrichment of the Au-Ag-Cu-Mo-Bi element association and could be used as an efficient exploration clue to delineate the exploration targets of skarn Cu mineralization.

The recognized exploration criteria, however, are limited to district-scale interpretations. This is due to the absence of local exploration evidence data to be incorporated in the recognition of exploration criteria of skarn Cu deposits (cf. Kreuzer et al., 2007; Carranza, 2008, 2009a; Lisitsin, 2015; Haddad-Martim et al., 2017). Besides, the suggested criteria were developed and thus are limited to the available data, and they can be further facilitated using supplemental data sets. Although, the study area of this paper is situated in a forest region, in which dense vegetation makes it extremely challenging to extract hydrothermally altered zones through satellite imaginary data. Moreover, the study area lacks detail airborne geophysical data.

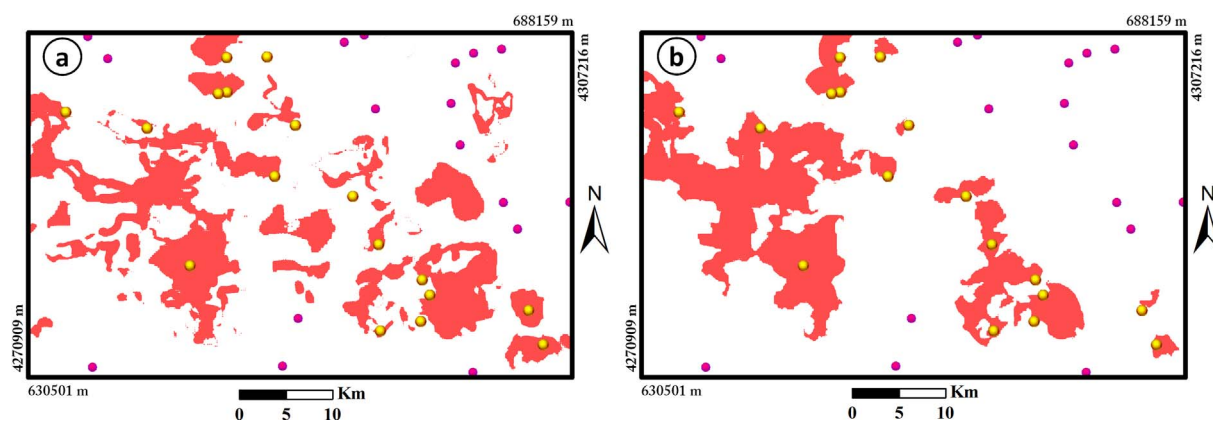Categorization of spatial evidence values into crisp classes often

Fig. 16. Exploration targets (red polygons) delineated by (a) LR and (b) RF prospectivity models. The yellow and purple circles are skarn-deposit and non-deposit locations, respectively. (For interpretation of the references to colour in this figure legend, the reader is referred to the web version of this article.)
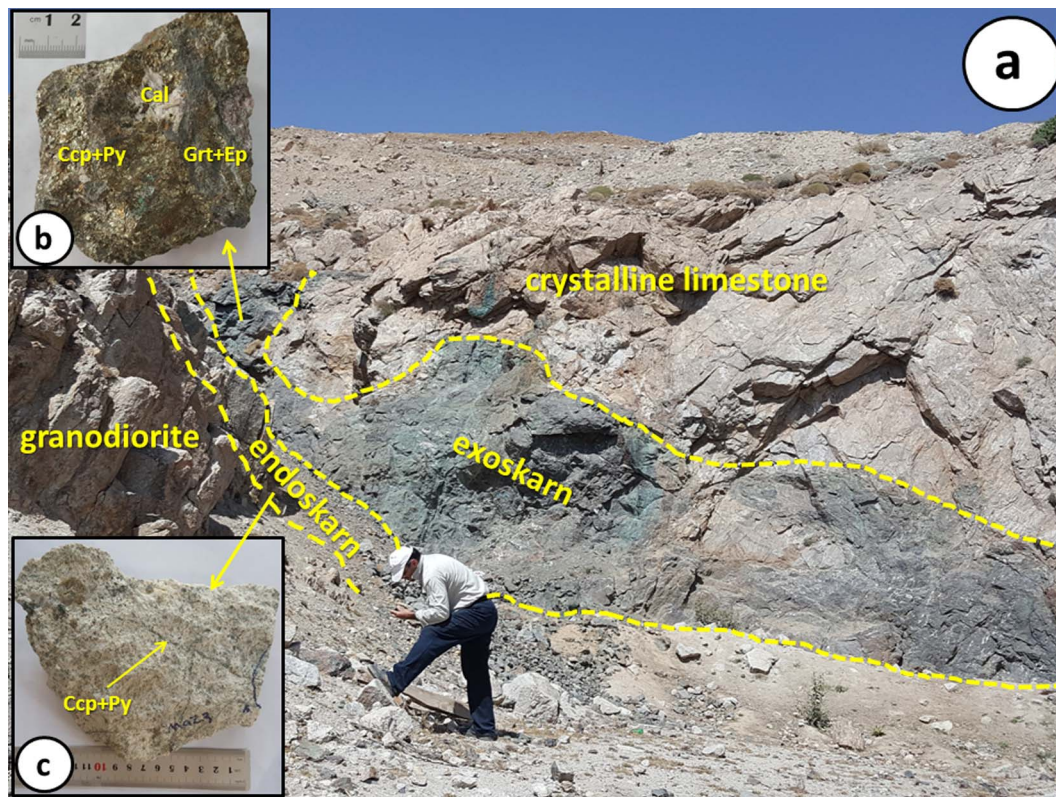
Fig. 17. Pieces of evidence of copper mineralization observed in the delineated exploration targets: (a) a granodiorite stock intruded within Cretaceous limestone, (b) hand specimen taken from exoskarn and (c) endoskarn zones manifesting Cu mineralization in the form of chalcopyrite. Cal: calcite; Ccp: chalcopyrite; Ep: epidote; Grt: garnet; Py: pyrite.
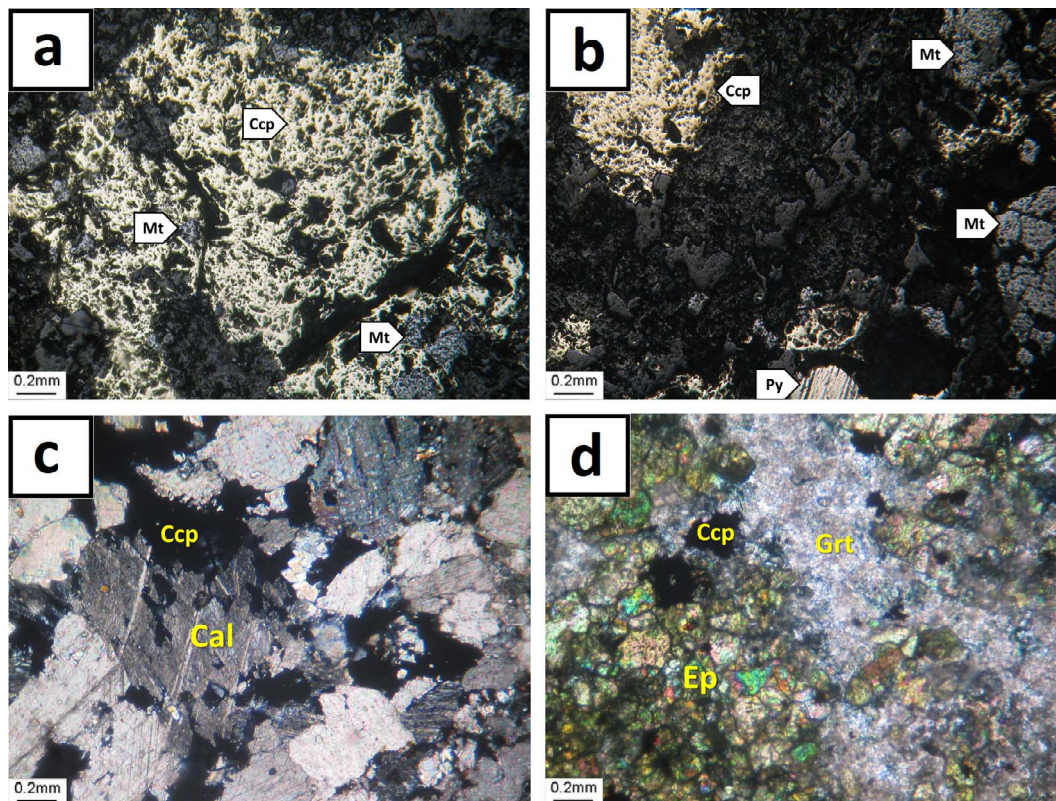

Fig. 18. Photographs of polished (a, b) and thin (c, d) sections from an observed exoskarn zone showing copper mineralization. Ccp: chalcopyrite; Mt: magnetite; Py: pyrite; Cal: calcite; Ep: epidote; Grt: garnet.

yields in loss of valuable information and is a source of systematic uncertainty in mineral prospectivity modeling (Porwal et al., 2003). To address this caveat, following Nykänen et al. (2008a,b, 2015) and Yousefi and Carranza (2015a,b, 2016), continuous evidence layers were employed in two modeling methods of this study. Furthermore, different methods of weighting and synthesizing exploration evidence data yield in various prospectivity models. Thus, as Carranza (2008) mentioned, at least two models should be generated and compared to select the superior one (e.g., Carranza and Laborte, 2015a,b; Zuo et al., 2015; Parsa et al., 2017a). In this study, because of higher success and prediction rates (Fig. 14), the random forest algorithm is found to be superior to the logistic regression for modeling the prospectivity of the skarn deposits. Therefore, the generated targets using random forest algorithm are reliable to follow exploration up.

Acknowledgment

References

Aghazadeh, M., Hou, Z., Badrzadeh, Z., Zhou, L., 2015. Temporal–spatial distribution and tectonic setting of porphyry copper deposits in Iran: constraints from zircon U-Pb and molybdenite Re–Os geochronology. Ore Geol. Rev. 70, 385–406.

Agterberg, F.P., Bonham-Carter, G.F., 2005. Measuring the performance of mineral-potential maps. Nat. Resour. Res. 14, 1–17.

Aitchison, J., 1986. The Statistical Analysis of Compositional Data. Chapman and Hall, London, pp. 416.

Alavi, M., 1994. Tectonics of the Zagros orogenic belt of Iran: new data and interpretations. Tectonophysics 229, 211–238.

Alavi, M., 2004. Regional stratigraphy of the Zagros fold-thrust belt of Iran and its proforeland evolution. Am. J. Sci. 304, 1–20.

Alavi, M., 2007. Structures of the Zagros fold-thrust belt in Iran. Am. J. Sci. 307, 1064–1095.

Andrada de Palomera, P., Van Ruitenbeek, F.J., Carranza, E.J.M., 2015. Prospectivity for epithermal gold-silver deposits in the Deseado Massif, Argentina. Ore Geol. Rev. 71, 484–501.

Asadi, H.H., Porwal, A., Fatehi, M., Kianpouryan, S., Lu, Y.J., 2015. Exploration feature selection applied to hybrid data integration modeling: Targeting copper-gold potential in central Iran. Ore Geol. Rev. 71, 819–838.

Asadi, H.H., Sansoleimani, A., Fatehi, M., Carranza, E.J.M., 2016. An AHP–TOPSIS predictive model for district-scale mapping of porphyry Cu–Au potential: a case study from Salafchegan Area (Central Iran). Nat. Resour. Res. 25, 417–429.

Baniadam, F., 2002. Study of geology and genesis of Au–Cu mineralization in the Nabijan area (M.Sc. thesis). Faculty of Earth Science, Geological Survey of Iran, Tehran (in Persian).

Baniadam, F., 2009. Assessing the Prospective Zones of Varzaghan District (Report). Geological Survey of Iran, Tehran (in Persian).

Berman, M., 1977. Distance distributions associated with Poisson processes of geometric figures. J. Appl. Probab. 14, 195–199.

Berman, M., 1986. Testing for spatial association between a point processes and another stochastic process. Appl. Stat. 35, 54–62.

Bonham-Carter, G.F., Goodfellow, W.D., 1984. Autocorrelation structure of stream sediment geochemical data: interpretation of Zn and Pb anomalies, Nahanni River area, Yukon-Northwest Territories, Canada. In: Verly, G., David, M., Journel, A.G., Marechal, A. (Eds.), Geostatistics for Natural Resources Characterization Part 2. D. Reidel, Dordrecht, pp. 817–829.

Bonham-Carter, G.F., Goodfellow, W.D., 1986. Background corrections to stream geochemical data using digitized drainage and geological maps: application to Selwyn Basin, Yuk on and Northwest Territories. J. Geochem. Explor. 25, 139–155.

Bonham-Carter, G.F., Agterberg, F.P., Wright, D.F., 1990. Weights of evidence modeling: a new approach to mapping mineral potential. Stat. Appl. Earth Sci. 89, 171–183.

Boots, B.N., Getis, A., 1988. Point Pattern Analysis. Sage University Scientific Geography Series No. 8. Sage Publications, Beverly Hills, pp. 93.

Breiman, L., 1984. Classification and Regression Trees. Chapman & Hall/CRC, London.

Breiman, L., 1996. Bagging predictors. Mach. Learn. 24, 123–140.

Breiman, L., 2001. Random forests. Mach. Learn. 45, 5–32.

Burt, D.M., 1977. Mineralogy and petrology of skarn deposits. Soc. Ital. Miner. Petrol Rend. 33, 859–873.

Calagari, A.A., Hosseinzadeh, G., 2006. The mineralogy of copper-bearing skarn to the east of the Sungun-Chay river, East-Azarbaidjan, Iran. J. Asian Earth Sci. 28, 423–438.

Carlson, C.A., 1991. Spatial distribution of ore deposits. Geology 19, 111–114.

Carranza, E.J.M., 2008. Geochemical Anomaly and Mineral Prospectivity Mapping in GIS Vol. 11 Elsevier, Amsterdam.

Carranza, E.J.M., 2009a. Controls on mineral deposit occurrence inferred from analysis of their spatial pattern and spatial association with geological features. Ore Geol. Rev. 35, 383–400.

Carranza, E.J.M., 2009b. Objective selection of suitable unit cell size in data-driven modeling of mineral prospectivity. Comput. Geosci. 35, 2032–2046.

Carranza, E.J.M., 2010. Mapping of anomalies in continuous and discrete fields of stream sediment geochemical landscapes. Geochem. Explor. Environ. Anal. 10, 171–187.

Carranza, E.J.M., Laborte, A.G., 2015a. Data-driven predictive mapping of gold prospectivity, Baguio district, Philippines: Application of Random Forest algorithm. Ore Geol. Rev. 71, 777–787.

Carranza, E.J.M., Laborte, A.G., 2015b. Random forest predictive modeling of mineral prospectivity with small number of prospects and data with missing values in Abra (Philippines). Comput. Geosci. 74, 60–70.

Carranza, E.J.M., Laborte, A.G., 2016. Data-driven predictive modeling of mineral prospectivity using random forest: a case study in Catanduanes Island (Philippines). Nat. Resour. Res. 25, 35–50.

Carranza, E.J.M., Sadeghi, M., 2010. Predictive mapping of prospectivity and quantitative estimation of undiscovered VMS deposits in Skellefte district (Sweden). Ore Geol. Rev. 38, 219–241.

Carranza, E.J.M., Hale, M., Faassen, C., 2008. Selection of coherent deposit-type locations and their application in data-driven mineral prospectivity mapping. Ore Geol. Rev. 33, 536–558.

Carranza, E.J.M., Owusu, E.A., Hale, M., 2009. Mapping of prospectivity and estimation of number of undiscovered prospects for lode gold, southwestern Ashanti Belt, Ghana. Miner. Deposita 44, 915–938.

Cheng, Q., Agterberg, F.P., 1995. Multifractal modeling and spatial point processes. Math. Geol. 27, 831–845.

Cheng, Q., Agterberg, F.P., Bonham-Carter, G.F., 1996. Fractal pattern integration for mineral potential estimation. Nonrenewable Resour. 5, 117–130.

Cheng, Q., Xia, Q., Li, W., Zhang, S., Chen, Z., Zuo, R., Wang, W., 2010. Density/area power-law models for separating multi-scale anomalies of ore and toxic elements in stream sediments in Gejiu mineral district, Yunnan Province, China. Biogeosciences 7, 3019–3025.

Chung, C.F., Agterberg, F.P., 1980. Regression models for estimating mineral resources from geological map data. Math. Geol. 12, 473–488.

Chung, C.J.F., Fabbri, A.G., 2003. Validation of spatial prediction models for landslide hazard mapping. Nat. Hazards 30, 451–472.

Cox, D.P., Singer, D.A., 1986. Mineral Deposit Models. U.S. Geological Survey Bulletin 1693. United States Government Printing Office, Washington.

Cox, D.R., Snell, E.J., 1989. Analysis of Binary Data, second ed. Chapman and Hall, London, pp. 236.

Cox, S.F., Etheridge, M.A., Wall, V.J., 1987. The role of fluids in syntectonic mass transport, and the localization of metamorphic vein-type ore deposists. Ore Geol. Rev. 2, 65–86.

Diggle, P.J., 1983. Statistical Analysis of Spatial Point Patterns. Academic Press, London, pp. 148.

Diggle, P.J., 2003. Statistical Analysis of Spatial Point Patterns. Arnold Publishers, London, pp. 159.

Egozcue, J.J., Pawlowsky-Glahn, V., Mateu-Figueras, G., Barcelo-Vidal, C., 2003. Isometric logratio transformations for compositional data analysis. Math. Geol. 35, 279–300.

Fabbri, A.G., Chung, C.J., 2008. On blind tests and spatial prediction models. Nat. Resour. Res. 17, 107–118.

Fatehi, M., Asadi, H.H., 2017a. Data integration modeling applied to drill hole planning through semi-supervised learning: A case study from the Dalli Cu-Au porphyry deposit in the central Iran. J. Afr. Earth Sc. 128, 147–160.

Fatehi, M., Asadi, H.H., 2017b. Application of semi-supervised fuzzy c-means method in clustering multivariate geochemical data, a case study from the Dalli Cu-Au porphyry deposit in central Iran. Ore Geol. Rev. 81, 245–255.

Faulkner, D.R., Jackson, C.A.L., Lunn, R.J., Schlische, R.W., Shipton, Z.K., Wibberley, C.A.J., Withjack, M.O., 2010. A review of recent developments concerning the structure, mechanics and fluid flow properties of fault zones. J. Struct. Geol. 32, 1557–1575.

Filzmoser, P., Hron, K., Reimann, C., Garrett, R., 2009. Robust factor analysis for compositional data. Comput. Geosci. 35, 1854–1861.

Ford, A., Blenkinsop, T.G., 2008. Combining fractal analysis of mineral deposit clustering with weights of evidence to evaluate patterns of mineralization: application to copper deposits of the Mount Isa Inlier, NW Queensland, Australia. Ore Geol. Rev. 33, 435–450.

Fry, N., 1979. Random point distributions and strain measurement in rocks. Tectonophysics 60, 89–105.

Glennie, K.W., 2000. Cretaceous tectonic evolution of Arabia's eastern plate margin: a tale of two oceans. Soc. Sediment. Geol. Special Publ. 26, 9–20.

Haddad-Martim, P.M., de Souza Filho, C.R., Carranza, E.J.M., 2017. Spatial analysis of mineral deposit distribution: A review of methods and implications for structural controls on iron oxide-copper-gold mineralization in Carajás, Brazil. Ore Geol. Rev. 81, 230–244.

Hassanpour, S., 2013. The alteration, mineralogy and geochronology (SHRIMP U-Pb and 40Ar/39Ar) of copper-bearing Anjerd skarn, north of the Shayvar Mountain, NW Iran. Int. J. Earth Sci. 102, 687–699.

Hezarkhani, A., Williams-Jones, A.E., 1998. Controls of alteration and mineralization in the Sungun porphyry copper deposit, Iran; evidence from fluid inclusions and stable isotopes. Econ. Geol. 93, 651–670.

Hosmer, D.W., Lemeshow, S., 2000. Applied Logistic Regression, second ed. John Wiley & Sons, New York, pp. 392.

Isham, V., 2010. Spatial point process models. In: Gelfand, A.E., Diggle, P.J., Fuentes, M., Guttorp, P. (Eds.), Handbook of Spatial Statistics. CRC Press, pp. 283–298.

Jamali, H., Mehrabi, B., 2015. Relationships between arc maturity and Cu–Mo–Au porphyry and related epithermal mineralization at the Cenozoic Arasbaran magmatic belt. Ore Geol. Rev. 65, 487–501.

Jamali, H., Dilek, Y., Daliran, F., Yaghubpur, A., Mehrabi, B., 2010. Metallogeny and tectonic evolution of the Cenozoic Ahar-Arasbaran volcanic belt, northern Iran. Int. Geol. Rev. 52, 608–630.

Kaiser, H.F., 1958. The varimax criterion for analytic rotation in factor analysis. Psychometrika 23, 187–200.

Karimzadeh Somarin, A., 2004a. Garnet composition as an indicator of Cu mineralization: evidence from skarn deposits of NW Iran. J. Geochem. Explor. 81, 47–57.

Karimzadeh Somarin, A., 2004b. Geochemical effects of endoskarn formation in the Mazraeh Cu–Fe skarn deposit in northwestern Iran. Geochem. Explor. Environ. Anal. 4, 307–315.

Karimzadeh Somarin, A., Moayyed, M., 2002. Granite-and gabbrodiorite-associated skarn deposits of NW Iran. Ore Geol. Rev. 20, 127–138.

Kreuzer, O.P., Blenkinsop, T.G., Morrison, R.J., Peters, S.G., 2007. Ore controls in the Charters Towers goldfield, NE Australia: Constraints from geological, geophysical and numerical analyses. Ore Geol. Rev. 32, 37–80.

Liaw, A., Wiener, M., 2002. Classification and regression by randomForest. R news 2, 18–22.

Lindsay, M., Aitken, A., Ford, A., Dentith, M., Hollis, J., Tyler, I., 2016. Reducing subjectivity in multi-commodity mineral prospectivity analyses: modeling the west Kimberley, Australia. Ore Geol. Rev. 76, 395–413.

Lisitsin, V., 2015. Spatial data analysis of mineral deposit point patterns: applications to exploration targeting. Ore Geol. Rev. 71, 861–881.

Maghsoudi, A., Yazdi, M., Mehrpartou, M., Vosoughi, M., Younesi, S., 2014. Porphyry Cu–Au mineralization in the Mirkuh Ali Mirza magmatic complex, NW Iran. J. Asian Earth Sci. 79, 932–941.

Mandelbrot, B.B., 1983. The Fractal Geometry of Nature. Freeman, New York, pp. 495.

McCuaig, T.C., Beresford, S., Hronsky, J., 2010. Translating the mineral systems approach into an effective exploration targeting system. Ore Geol. Rev. 38, 128–138.

Mehrpartou, M., Nazer, N.K.H., 1999. Geological Map of Iran 1: 100,000 Series. Geological Survey of Iran, Kalibar, Tehran.

Mehrpartou, M., Aminifazl, A., Radfar, J., 1992. Geological Map of Iran 1: 100,000 Series. Geological Survey of Iran, Varzaghan, Tehran.

Meinert, L.D., 1992. Skarns and skarn deposits. Geosci. Can. 19, 145–162.

Meinert, L.D., Hedenquist, J.W., Satoh, H., Matsuhisa, Y., 2003. Formation of anhydrous and hydrous skarn in Cu-Au ore deposits by magmatic fluids. Econ. Geol. 98, 147–156.

Meinert, L.D., Dipple, G.M., Nicolescu, S., 2005. World skarn deposits. Econ. Geol. 100, 299–336.

Menard, S., 2001. Applied Logistic Regression Analysis. Sage University Papers Series on Quantitative Applications in the Social Sciences, Vol. 07–106. Sage Thousand Oaks, California, pp. 128.

Meshkani, S.A., Mehrabi, B., Yaghubpur, A., Sadeghi, M., 2013. Recognition of the regional lineaments of Iran: Using geospatial data and their implications for exploration of metallic ore deposits. Ore Geol. Rev. 55, 48–63.

Micheletti, N., Foresti, L., Robert, S., Leuenberger, M., Pedrazzini, A., Jaboyedoff, M., Kanevski, M., 2014. Machine learning feature selection methods for landslide susceptibility mapping. Math. Geosci. 46, 33–57.

Mokhtari, A.R., 2014. Hydrothermal alteration mapping through multivariate logistic regression analysis of lithogeochemical data. J. Geochem. 145, 207–212.

Mokhtari, A.R., Rodsari, P.R., Fatehi, M., Shahrestani, S., Pournik, P., 2014. Geochemical prospecting for Cu mineralization in an arid terrain-central Iran. J. Afr. Earth Sc. 100, 278–288.

Mokhtari, M.A.A., Ebrahimi, M., Ghorbani, M.R., 2017. Mineralogy and skarnification processes at the Avan Cu-Fe Skarn, northeast of Kharvana, NW Iran. J. Econ. Geol. 8, 359–380.

Mollai, H., Sharma, R., Pe-Piper, G., 2009. Copper mineralization around the Ahar batholith, north of Ahar (NW Iran): evidence for fluid evolution and the origin of the skarn ore deposit. Ore Geol. Rev. 35, 401–414.

Mollai, H., Pe-Piper, G., Dabiri, R., 2014. Genetic relationships between skarn ore deposits and magmatic activity in the Ahar region, Western Alborz, NW Iran. Geol. Carpath. 65, 209–227.

Nykänen, V., Groves, D.I., Ojala, V.J., Gardoll, S.J., 2008a. Combined conceptual/empirical prospectivity mapping for orogenic gold in the northern Fennoscandian Shield, Finland. Aust. J. Earth Sci. 55, 39–59.

Nykänen, V., Groves, D.I., Ojala, V.J., Eilu, P., Gardoll, S.J., 2008b. Reconnaissance-scale conceptual fuzzy-logic prospectivity modelling for iron oxide copper–gold deposits in the northern Fennoscandian Shield, Finland. Aust. J. Earth Sci. 55, 25–38.

Nykänen, V., Lahti, I., Niiranen, T., Korhonen, K., 2015. Receiver operating characteristics (ROC) as validation tool for prospectivity models—a magmatic Ni–Cu case study from the Central Lapland Greenstone Belt, Northern Finland. Ore Geol. Rev. 71, 853–860.

Parsa, M., Maghsoudi, A., Yousefi, M., Sadeghi, M., 2016a. Recognition of significant multi-element geochemical signatures of porphyry Cu deposits in Noghdouz area, NW Iran. J. Geochem. Explor. 165, 111–124.

Parsa, M., Maghsoudi, A., Yousefi, M., Sadeghi, M., 2016b. Prospectivity modeling of porphyry-Cu deposits by identification and integration of efficient mono-elemental geochemical signatures. J. Afr. Earth Sci. 114, 228–241.

Parsa, M., Maghsoudi, A., Ghezelbash, R., 2016c. Decomposition of anomaly patterns of multi-element geochemical signatures in Ahar area, NW Iran: a comparison of U-spatial statistics and fractal models. Arabian J. Geosci. 9, 1–16.

Parsa, M., Maghsoudi, A., Yousefi, M., 2017a. An improved data-driven fuzzy mineral prospectivity mapping procedure: cosine amplitude-based similarity approach to delineate exploration targets. Int. J. Appl. Earth Obs. Geoinf. 58, 157–167.

Parsa, M., Maghsoudi, A., Yousefi, M., Carranza, E.J.M., 2017b. Multifractal interpolation and spectrum–area fractal modeling of stream sediment geochemical data: Implications for mapping exploration targets. J. Afr. Earth Sci. 128, 5–15.

Parsa, M., Maghsoudi, A., Yousefi, M., Sadeghi, M., 2017c. Multifractal analysis of stream sediment geochemical data: Implications for hydrothermal nickel prospection in an arid terrain, eastern Iran. J. Geochem. Explor. http://dx.doi.org/10.1016/j.gexplo.2016.11.013.

Parsa, M., Maghsoudi, A., Carranza, E.J.M., Yousefi, M., 2017d. Enhancement and Mapping of Weak Multivariate Stream Sediment Geochemical Anomalies in Ahar Area, NW Iran. Nat. Resour. Res. 26, 443–455.

Parsa, M., Maghsoudi, A., Yousefi, M., 2017e. A receiver operating characteristics-based geochemical data fusion technique for targeting undiscovered mineral deposits. Nat. Resour. Res. http://dx.doi.org/10.1007/s11053-017-9351-6.

Pirajno, F., 1992. Hydrothermal Mineral Deposits, Principles and Fundamental Concepts for the Exploration Geologists. Springer-Verlag, Berlin.

Pison, G., Rousseeuw, P.J., Filzmoser, P., Croux, C., 2003. Robust factor analysis. J. Multivariate Anal. 84, 145–172.

Porwal, A., Carranza, E.J.M., Hale, M., 2003. Knowledge-driven and data-driven fuzzy models for predictive mineral potential mapping. Nat. Resour. Res. 12, 1–25.

Pourghasemi, H.R., Kerle, N., 2016. Random forests and evidential belief function-based landslide susceptibility assessment in Western Mazandaran Province, Iran. Environ. Earth Sci. 75, 1–17.

R Development core team. 2008. The R project for statistical computing. http://www.R-project.org.

Raines, G.L., 2008. Are fractal dimensions of the spatial distribution of mineral deposits meaningful? Nat. Resour. Res. 17, 87–97.

Reimann, C., Filzmoser, P., Garrett, R.G., 2002. Factor analysis applied to regional geochemical data: problems and possibilities. Appl. Geochem. 17, 185–206.

Richards, J.P., Spell, T., Rameh, E., Razique, A., Fletcher, T., 2012. High Sr/Y magmas reflect arc maturity, high magmatic water content, and porphyry Cu ± Mo ± Au potential: examples from the Tethyan arcs of Central and Eastern Iran and Western Pakistan. Econ. Geol. 107, 295–332.

Roberts, R.G., Sheahan, P., Cherry, M.E., 1988. Ore Deposit Models, Geoscience Canada Reprint Series 3. Geological Association of Canada, Newfoundland.

Rodriguez-Galiano, V., Sanchez-Castillo, M., Chica-Olmo, M., Chica-Rivas, M., 2015. Machine learning predictive models for mineral prospectivity: An evaluation of neural networks, random forest, regression trees and support vector machines. Ore Geol. Rev. 71, 804–818.

Spadoni, M., 2006. Geochemical mapping using a geomorphologic approach based on catchments. J. Geochem. Explor. 90, 183–196.

Spadoni, M., Voltaggio, M., Cavarretta, G., 2005. Recognition of areas of anomalous concentration of potentially hazardous elements by means of a subcatchmentbased discriminant analysis of stream sediments. J. Geochem. Explor. 87, 83–91.

Thompson, M., Howarth, R.J., 1976. Duplicate analysis in geochemical practice. Part I. Theoretical approach and estimation of analytical reproducibility. Analyst 101, 690–698.

Treiblmaier, H., Filzmoser, P., 2010. Exploratory factor analysis revisited: How robust methods support the detection of hidden multivariate data structures in IS research. Inf. Manage. 47, 197–207.

Vearncombe, J., Vearncombe, S., 1999. The spatial distribution of mineralization; applications of Fry analysis. Econ. Geol. 94, 475–486.

Yousefi, M., 2017. Recognition of an enhanced multi-element geochemical signature of porphyry copper deposits for vectoring into mineralized zones and delimiting exploration targets in Jiroft area, SE Iran. Ore Geol. Rev. 83, 200–214.

Yousefi, M., Carranza, E.J.M., 2015. Prediction-area (P-A) plot and C-A fractal analysis to classify and evaluate evidential maps for mineral prospectivity modeling. Comput. Geosci. 79, 69–81.

Yousefi, M., Carranza, E.J.M., 2015a. Fuzzification of continuous-value spatial evidence for mineral prospectivity mapping. Comput. Geosci. 74, 97–109.

Yousefi, M., Carranza, E.J.M., 2016. Union score and fuzzy logic mineral prospectivity mapping using discretized and continuous spatial evidence values. J. Afr. Earth Sc. 128, 47–60.

Yousefi, M., Carranza, E.J.M., Kamkar-Rohani, A., 2013. Weighted drainage catchment basin mapping of geochemical anomalies using stream sediment data for mineral potential modeling. J. Geochem. Explor. 128, 88–96.

Yousefi, M., Kamkar-Rouhani, A., Carranza, E.J.M., 2014. Application of staged factor analysis and logistic function to create a fuzzy stream sediment geochemical evidence layer for mineral prospectivity mapping. Geochem. Explor. Environ. Anal. 14, 45–58.

Zarasvandi, A., Rezaei, M., Sadeghi, M., Lentz, D., Adelpour, M., Pourkaseb, H., 2015. Rare earth element signatures of economic and sub-economic porphyry copper systems in Urumieh-Dokhtar Magmatic Arc (UDMA), Iran. Ore Geol. Rev. 70, 407–423.

Zuo, R., Agterberg, F.P., Cheng, Q., Yao, L., 2009. Fractal characterization of the spatial distribution of geological point processes. Int. J. Appl. Earth Obs. Geoinf. 11, 394–402.

Zuo, R., Zhang, Z., Zhang, D., Carranza, E.J.M., Wang, H., 2015. Evaluation of uncertainty in mineral prospectivity mapping due to missing evidence: a case study with skarn-type Fe deposits in Southwestern Fujian Province, China. Ore Geol. Rev. 71, 502–515.